The Dissertation Committee for Robert Vincent Crawford certifies that this is the approved version of the following dissertation:

Passive Pumping, Evaporation Based System for Multiscale Thermal Management

Committee:

Alexandre K. da Silva, Supervisor

Halil Berberoglu

David Bogard

Atila Novoselac

Michael Webber

Passive Pumping, Evaporation Based System for Multiscale Thermal Management

by

Robert Vincent Crawford, B.S.M.E; M.S.

Dissertation

Presented to the Faculty of the Graduate School of

The University of Texas at Austin

in Partial Fulfillment

of the Requirements

for the Degree of

Doctor of Philosophy

The University of Texas at Austin

August 2013

Dedication

This dissertation is dedicated to my family for the love and support they have shown me throughout my graduate studies. To my parents, Gina and Howard, by word and example, you have instilled in me the lessons and value of honor, integrity, morality and love. To my loving brother, Nicholas, your support has been immense and appreciated. To my dog, Penny, you have brought so much joy into my life.

To Girolama, this dissertation is especially dedicated to you. Your love and encouragement has made this all possible. Even though we have been separated by great distances, we have grown ever closer. I am finally coming home to you.

"Fix reason firmly in her set, and call to her tribunal every fact, every opinion. Question with boldness even the existence of a God; because, if there be one, he must more approve of the homage of reason, than that of blindfolded fear."

- *Thomas Jefferson*

Acknowledgements

My gratitude goes to my advisor, Dr. Alexandre K. da Silva, for his guidance and support. Thank you for the opportunity to work with you.

I would like to thank Dr. Halil Berberoglu, Dr. David Bogard, Dr. Atila Novoselac and Dr. Michael Webber for their participation in my doctoral committee. They have provided valued insight and alternative perspectives.

I would like to thank my friends and colleagues at The University of Texas at Austin.

I thank the NSF IGERT program for the funding support.

I would like to thank Thomas Baldassare, Alicia Chojnowski and Patrick Michael Calkins. Texas has been an adventure. Tom, you are a brother to me.

Passive Pumping, Evaporation Based System for Multiscale Thermal Management

Robert Vincent Crawford, Ph.D.

The University of Texas at Austin, 2013

Supervisor: Alexandre K. da Silva

Drawing from the lessons of plant transpiration, this dissertation explores a biomimiced system for fluid transport and thermal regulation. This system utilizes evaporation and benefits from the associated passive pumping with an application of a rooftop solar radiation barrier in mind. By directing the incoming energy towards the phase change of water, lower surface temperatures can be maintained thus reducing heat transfer into the structure by conduction. In order to design and construct such a bio-inspired system, several parameters, i.e., the evaporation surface, the delivery path and the working fluid, must be understood as to how they affect and limit operations. Performance factors such as evaporation rate and suction pressure were monitored for the various design constraints of feeding tube length and diameter, membrane area, and working fluid. Additionally, as a heat flux was imposed on the membrane from above and below, the substrate temperature became important. Over the range of parameters tested, hydrodynamic resistances of the delivery path were shown to affect pumping height but not the evaporation rate. Instead, the evaporation rate was controlled by the substrate temperature. Furthermore, the normalized evaporation rate was found to be inversely

related to the evaporation surface area. Under contaminated working fluid conditions, particles deposited in the membrane caused decreases in evaporation rates. When applied to a simulated roof situation, the evaporation system was successful at maintaining considerably lower surface temperatures than other conventional and unconventional roof albedos, which, in turn, would reduce heat flux into the interior by conduction. Lastly, in estimating the water consumption, on a typical August day in Austin, TX, the system could use up to 2 gallons/m^2 while providing enhanced cooling. When the system's resources were compared to being purposed in other ways, they were arguably better utilized in providing evaporative cooling.

Table of Contents

List of Tables

List of Figures

Nomenclature

c_p	specific heat	kJ/kg/K
g	gravitational acceleration	m/s^2
H	Height	m of water
K_p	Permeability	m^2
$\dot{m}$	Mass Flow Rate	kg/s
q	Flow Rate	m/s
q	Heat Flux	W/m^2
P	Pressure	Pa
T	Temperature	K (°C)
ρ	Density	gm/cm^3
μ	Viscosity	Pa·s
∇	Gradient	dimensionless

Chapter 1. Introduction

The processes of nature have been a great source of inspiration for man; perhaps the most famous being man's desire to fly. Based on the study and imitation of nature's systems, the field received its identifying name, biomimetics, from Otto Schmitt in the 1950's [1, 2]. Of interest in this dissertation is biomimicing the process of transpiration in plants for passive fluid transport and thermal assistance with the motivation of reducing energy consumption related to building cooling. Therefore, below, the following topics are reviewed to show the extent of existing work related to transpiration biomimicry, the energy intensity of building cooling in the commercial sector, evaporation work related to roof thermal shielding and the basics of capillary transport which will be utilized in fluid transport in the proposed system's evaporative membrane.

1.1 Transpiration Background

Transpiration is the passive flow of water in plants from the soil to the atmosphere. In plants, whose height is greater than the capability of capillary action to overcome gravity, transpiration is relied on for moving water and minerals throughout the body via xylem [3], as depicted in Figure 1.1 [4]. The transpiration process begins when plants take in carbon dioxide for photosynthesis through pores on the underside of the leaves called stomata. During this process, water vapor escapes, generating a suction pressure, which can be traced through the plant body, down to the root system, which in turn brings in water from the soil. As the water flows inward, it brings dissolved minerals from the soil, which is vital to the health of the plant. Additionally, transpiration prevents leaves from overheating in direct sunlight [5, 6]. One of the main advantages of transpiration is that it is a passive evaporative pumping operation that does not require the assistance of pumps, valves or moving parts, making it a robust system with diminished maintenance requirements.

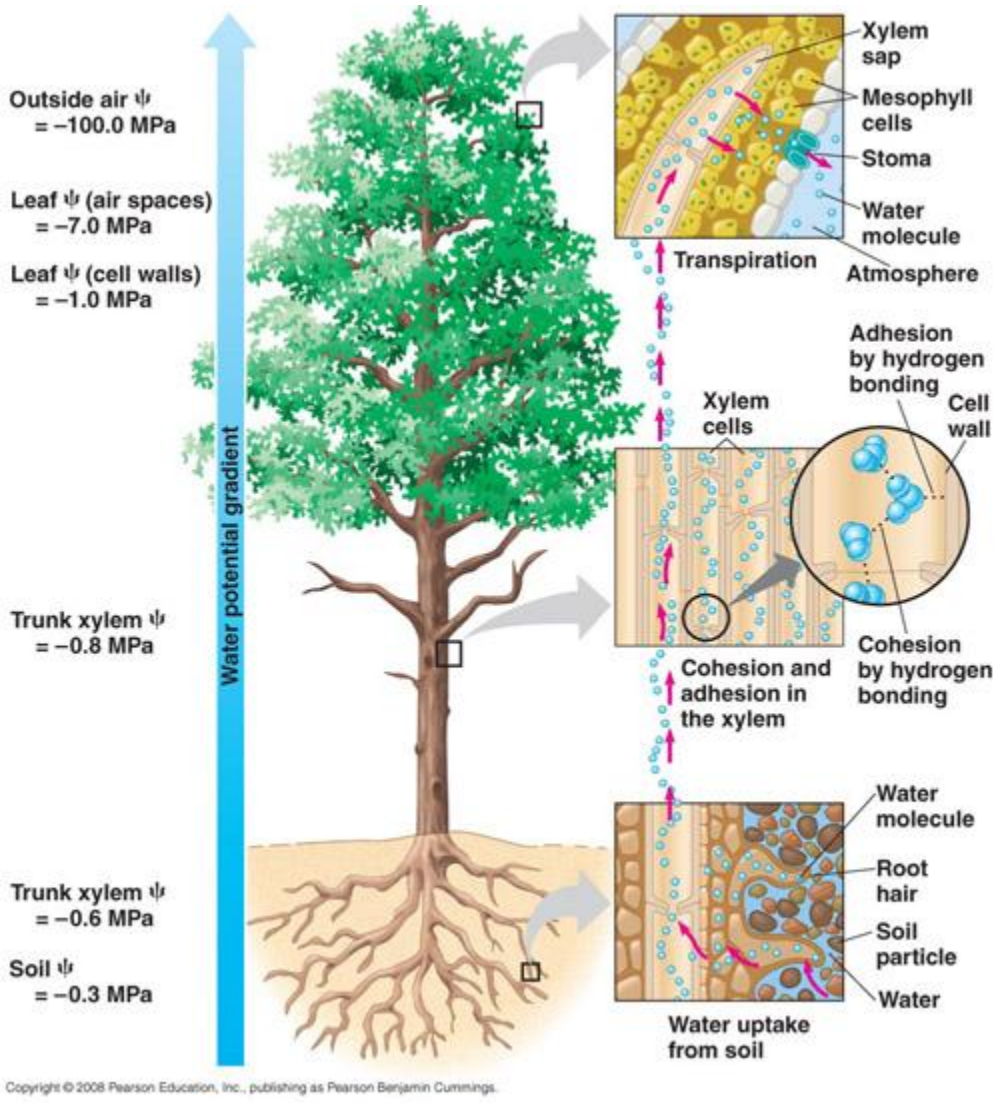

Fig. 1.1: Movement of water through a plant [4].

According to Dixon and Joly's Cohesion Theory [7], suction pressures up to –1.0 MPa can be imposed by root systems, pulling water from the soil to replenish what had been evaporated from the leaves [8, 9]; a good example being the redwood trees of the Pacific Northwest, which can be over 100 meters high [10].Since the development of Cohesion Theory, more extensive investigations have been conducted showing that fluid ascension to the top of plants involves more than evaporation generated tensile forces [11]. While studying the herbaceous plants and trees, *in situ* measurements of capillary

networks, less than 1 μm, and microporous structures have shown capillary forces can lift water as much as 100 m [12, 13]. Additionally, viscous polymeric compounds have been found in the vessels of plants which have shown to lift water [14, 15]. The presence of these compounds can create a convectional flow between xylem elements causing ascension. Negatively charged polymers attached to the xylem wall are also responsible for water movement by generating an electrical double layer [16, 17]. By creating a charged inner wall, gravitational gradients can be overcome up to 100 m. While the literature has shown that transpiration is actually more complicated and utilizes additional processes (e.g. evaporation, osmosis, wicking, and others) than Cohesion Theory first proposed [11], Cohesion Theory is a good basis for this research.

1.2 Energy Consumption Background

Buildings are subjected to solar heat fluxes, which are generally considered low when compared with dissipations in other applications. However, due to their footprint, they can receive large amounts of energy, which is transferred as heat to its structure. For commercial buildings, energy intensive air conditioning systems are needed to cool the interior space to provide a comfortable habitat for the workers and proper environmental conditions for the operation of equipment. As of 2011, the United States was consuming 97.3 Quadrillion Btu (Quads) annually from a variety of sources (i.e., fossil fuels, nuclear electric power, and renewable energy), Figure 1.2 [18]. Of the 18.02 Quads that went to the commercial sector, 14.5% of the energy went towards air conditioning, representing 2.64 Quads [19]. At energy demands this high, even single digit percentage decreases equate to large savings on both the user energy cost side and infrastructure capital cost side as well as lessening the impact of production on the environment.

With the commercial sector using roughly 18 Quads annually, 4 Quads comes from primary sources while the remaining comes from electricity [18]. From primary energy sources, the sector relies heavily on natural gas at 79%, with the remaining 21% being made up of petroleum at 17%, renewables at 3% and coal at 1%, [18]. Of electricity consumption, 4.5 Quads is actually used while the commercial sector's share

of conversion losses amounts to another 9.5 Quads, Figure 1.3 [18]. Whether it is the primary energy source of the commercial industry or the primary source of the electricity, each has its own drawback. Fossil fuels, for example, can have a negative impact on the environment and people's health with the emissions from combustion. While still highly toxic, spent nuclear fuel must be stored and safeguarded for hundreds of years. Even renewable sources have their own detrimental impacts. Hydroelectric power requires lakes, sometimes manmade, which can flood large tracts of land, destroying the ecosystem. Wind turbines have received complaints due to their visual proximity to affluent populations with people clinging to the "not in my back yard" (NIMBY) standard. Solar, too, has the drawback of being very land intensive due to its low efficiencies. Additionally, with wind and solar power, they are intermittent and must rely on as yet to be developed storage capabilities. Furthermore, wind and solar are generally most productive in geographical locations where people do not live thus the power must be transmitted great distances. However, even with small decreases in energy usage, there can be deep, directly felt impacts on the negative aspects of individual energy sources.

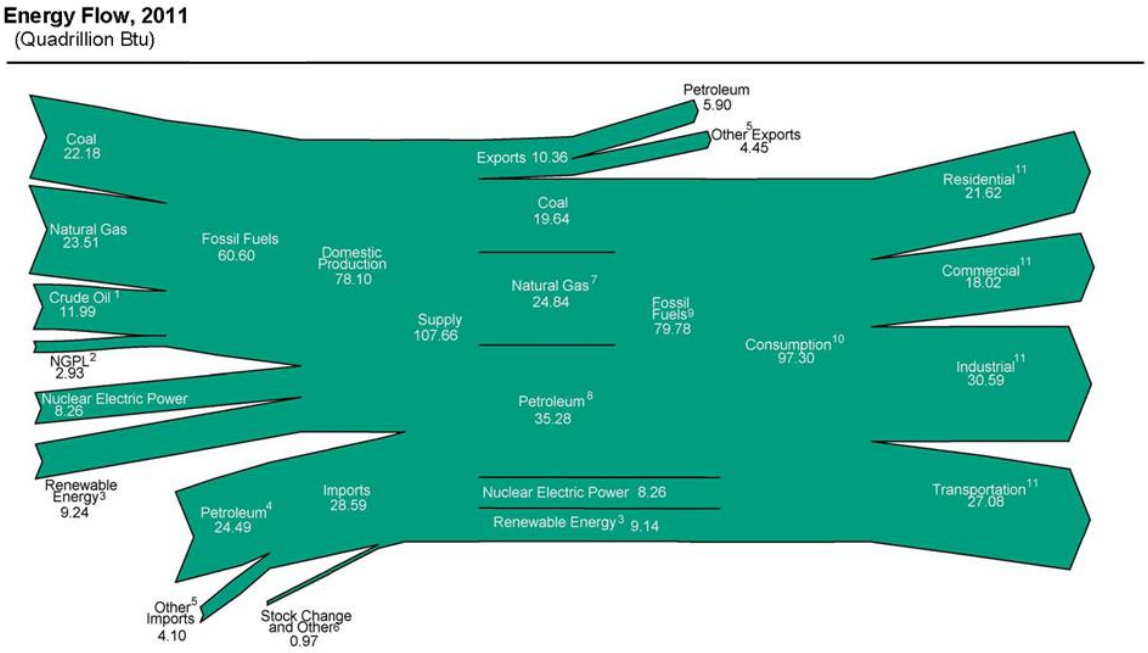

[1] Includes lease condensate.
[2] Natural gas plant liquids.
[3] Conventional hydroelectric power, biomass, geothermal, solar/photovoltaic, and wind.
[4] Crude oil and petroleum products. Includes imports into the Strategic Petroleum Reserve.
[5] Natural gas, coal, coal coke, biofuels, and electricity.
[6] Adjustments, losses, and unaccounted for.
[7] Natural gas only; excludes supplemental gaseous fuels.
[8] Petroleum products, including natural gas plant liquids, and crude oil burned as fuel.
[9] Includes 0.01 quadrillion Btu of coal coke net imports.
[10] Includes 0.13 quadrillion Btu of electricity net imports.
[11] Total energy consumption, which is the sum of primary energy consumption, electricity retail sales, and electrical system energy losses. Losses are allocated to the end-use sectors in proportion to each sector's share of total electricity retail sales. See Note, "Electrical Systems Energy Losses," at end of Section 2.
Notes: • Data are preliminary. • Values are derived from source data prior to rounding for publication. • Totals may not equal sum of components due to independent rounding.
Sources: Tables 1.1, 1.2, 1.3, 1.4, and 2.1a.

Fig. 1.2: 2011 energy flow to individual sectors for the U.S. Provided by the U.S. Energy Information Administration, Annual Energy Review 2011 [18].

Electricity Flow, 2011
(Quadrillion Btu)

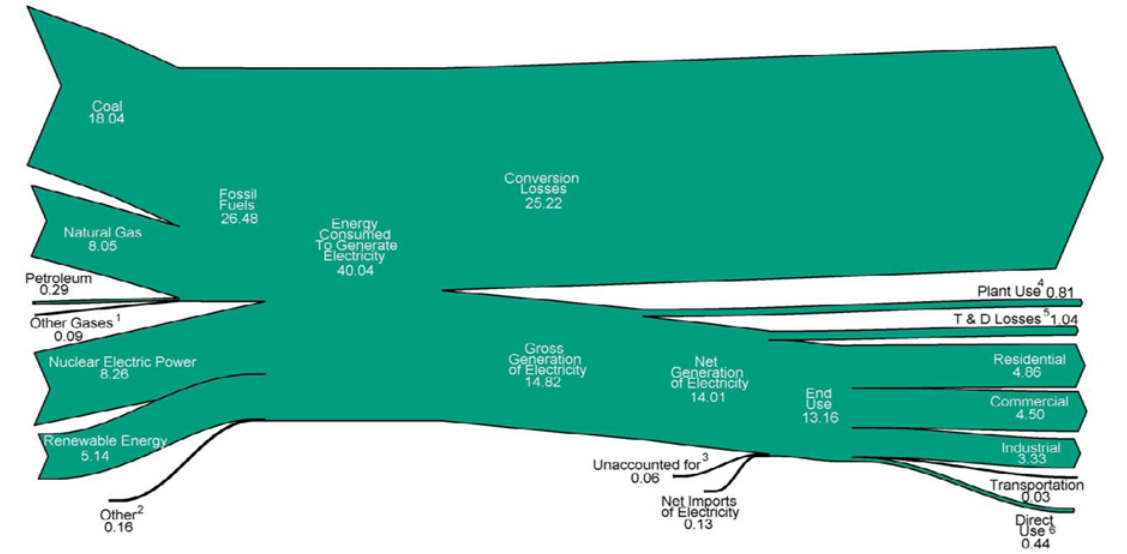

[1] Blast furnace gas, propane gas, and other manufactured and waste gases derived from fossil fuels.
[2] Batteries, chemicals, hydrogen, pitch, purchased steam, sulfur, miscellaneous technologies, and non-renewable waste (municipal solid waste from non-biogenic sources, and tire-derived fuels).
[3] Data collection frame differences and nonsampling error. Derived for the diagram by subtracting the "T & D Losses" estimate from "T & D Losses and Unaccounted for" derived from Table 8.1.
[4] Electric energy used in the operation of power plants.
[5] Transmission and distribution losses (electricity losses that occur between the point of generation and delivery to the customer) are estimated as 7 percent of gross generation.
[6] Use of electricity that is 1) self-generated, 2) produced by either the same entity that consumes the power or an affiliate, and 3) used in direct support of a service or industrial process located within the same facility or group of facilities that house the generating equipment. Direct use is exclusive of station use.

Notes: • Data are preliminary. • See Note, "Electrical System Energy Losses," at the end of Section 2. • Net generation of electricity includes pumped storage facility production minus energy used for pumping. • Values are derived from source data prior to rounding for publication. • Totals may not equal sum of components due to independent rounding.

Sources: Tables 8.1, 8.4a, 8.9, A6 (column 7), and U.S. Energy Information Administration, Form EIA-923, "Power Plant Operations Report."

Fig. 1.3: 2011 electricity flow to individual sectors for the U.S. Provided by the U.S. Energy Information Administration, Annual Energy Review 2011 [18].

1.3 Capillary Transport

The system developed in this dissertation is based on fluid transport to and evaporation from a membrane. In order to use membranes in such a capacity, one must keep in mind that membranes are an effective means of species separation in areas of water treatment [20, 21]. By their nature of contaminant removal from a flow, membranes are subject to fouling, or the deposition of solutes or particles thus degrading the performance of the membrane. Fouling can be thought of in two ways, external and internal. External fouling occurs when particulates which are too large to pass through the membrane, gathering on the top surface, whereas internal fouling contends with the buildup of foreign particles within the porous structure of the membrane [22].

Consequently, the life of a membrane can be shortened by fouling as it is based on the sustained ability to transmit fluid across the membrane with an accepted pressure drop. As flow rate is a function of permeability according to Darcy's law [23], Eq. 1.1, as fouling occurs on/in the membrane, permeability decreases cause a decrease in the flow rate,

$$q = \frac{-K_p}{\mu} \nabla P \tag{1.1}$$

where q is the flow flux, K_p is the permeability, μ is the viscosity, and ∇P is the pressure gradient.

Liquids in porous media, however, do not need a pressure gradient to drive the flow but rather can rely on wicking by capillary transport as shown by Washburn [24] in his fundamental investigation of small cylindrical capillaries. Additionally, because capillary flow is assumed to have a low Reynolds number, creep flow with the velocity profile being steady state, fully developed yields a transient process [25]. Because of this passive operation, it provides an alternative to using pumps to move fluid in increasingly smaller micro channels that have larger surface forces that must be overcome. This potential for fluid movement which normally would require great pumping efforts has attracted research from all scales, i.e., micro [26, 27], meso [28, 29] and molecular [30].

The applications for capillary transport are numerous. For thermal management of electronic devices, heat pipes rely on the capillary movement of fluid to transport heat for dissipation [31]. Ion transport has been studied in building physics [32]. During the drying process of porous materials such as concrete, ion crystallization can cause cracks and major structural issues. Capillary transport in surface functionalized paper can provide a low-cost and accurate means of rapid diagnosis in medical and forensics applications [33].

1.4 Biomimicing Transpiration

The passive operation of transpiration lends itself to the potential for many applications in fields that currently rely on micropumps for circulation, metering, and point to point transfer, e.g. biology [34], chemistry [35], microelectronics [36-38].

Wheeler and Stroock [9] recognized that a synthetic replica of a transpiration system had not yet been developed, as the techniques used in nature could not be matched. While the idea of biomimicing transpiration was to replicate a root network connected to a leaf membrane via a liquid-filled capillary, they cited the issue of not being able to identify materials with equal performance characteristics. To address this, they investigated using chemically cross-linked organic hydrogels as a membrane. Using this method, tension pressures in the liquid water were predicted in excess of -22 MPa. This confirmed that the hydrogel membrane could be used for driving fluid. They used soft lithography to construct the rest of their synthetic tree network in poly(hydroxyethyl methacrylate) (pHEMA) and bonded the hydrogel to the top of the channel network, Figure 1.4. Steady flow rates were achieved between the leaf structure exposed to an air stream and a root system exposed to liquid water. Having addressed the issue of creating a micro channel system utilizing evaporation driven flow, Wheeler and Stroock [9] tested their synthetic leaf when it was at elevated temperatures. As expected, the evaporation rates increased with increasing leaf temperatures. Accompanying the increase in flow rate was an increase in the calculated pressure drop between the root and leaf networks. The pressure drop in the system was calculated using the Navier-Stokes equations for laminar flow through a pipe where pressure drop was a function of flow rate. Direct measurements of pressure drop and suction pressure in a biomimiced transpiration system could not be found.

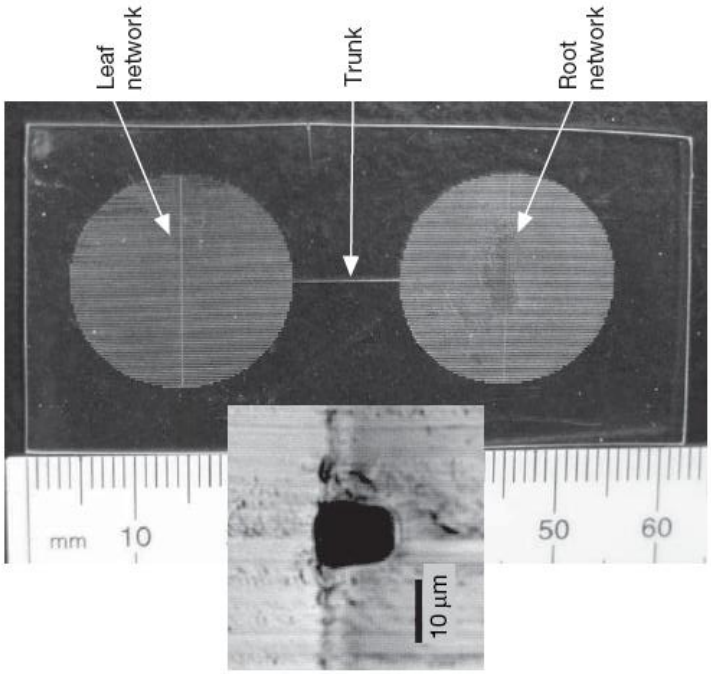

Fig. 1.4: Wheeler and Stroock's synthetic tree network [9].

Others too, with their own motives in mind, have used microfabrication to construct their own evaporation driven flow systems [10, 39-42]. Goedecke, et al. [10] used evaporation to drive flow with their biomimetic setup motivated by chromatography applications. Their microfabrication technique for making the micro channels was glass etching. As an air stream passed over an evaporation zone and subsequently, the fluid in that zone evaporated, more fluid was drawn through a micro channel from a liquid reservoir. Rather than using a porous membrane like others, they left the ends of their channels exposed to atmosphere. Additionally, they relied on capillary forces to help promote a continuous flow for which they observed velocities as high as 0.225 cm/s. Borno, et al. [39] used their own leaf structure to harvest energy from evaporation driven flows. In their setup, a micro channel stem connected a water reservoir and an etched microfluidic network. Embedded in the stem, Ti/Pt plates acted as parallel plate capacitors. As evaporation occurred from the micro channel network, fluid containing dielectric slugs was drawn through the stem generating a charge. Of importance, they

were able to attain flow velocities up to 1.5 cm/s. With an aim of controllable flow in mind, Nmasivayam, et al. [40] developed micro channels with hydrophobic patterns in order to pin the fluid meniscus and control evaporation rates. They wanted to precisely control flow at rates as low as 5 nL/min for possible usage in DNA and cell adhesion studies. To build the micro channels and hydrophobic patches, they used a hybrid system of both silicon and glass substrates with micro channels etched in using silanization. Also with DNA and cell adhesion studies in mind, Li, et al. [43] developed a transpiration based micropumping system that allowed for controllable, adjustable flow rates. Their fabrication technique was simpler than previously discussed works. They used a poly(vinyl chloride) (PVC) film bonded to a sheet of Poly(methyl methacrylate) (PMMA) with a commercially bought porous membrane underneath. They controlled evaporation rates by poking "stomata" holes into the PVC film with a 20 μm needle. Using flow visualization, they calculated controlled flow between 0.13 – 3.74 μL/min. Moreover, the effect of humidity on flow rate was investigated and found to be minimal below 70%. Guan, et al. [41, 42] used a porous filter paper as their evaporative membrane for their micropumping system, Figure 1.5. The filter paper was sandwiched between two PMMA plates, which had precut holes for evaporation. The pumping drew water through a micro channel that was etched into separate piece of glass. With 6.6 cm^2 of evaporation area, at a humidity of 30-32% and temperature of 20 - 21°C, they were able to sustain flow rates of 3μL/min. Furthermore, the system was able to pump with a height differential of 240 cm, analogous to 23.5 kPa. They investigated the effects of ambient relative humidity on their setup and found that in the mid range, flow rates saw a 1 to 3% decrease for each percent increase in humidity. Additionally, between 25 and 30 °C, each degree increase brought a 3% increase in flow rate. While all experienced some degree of success, the microfabrication techniques used to construct such devices are time consuming and expensive.

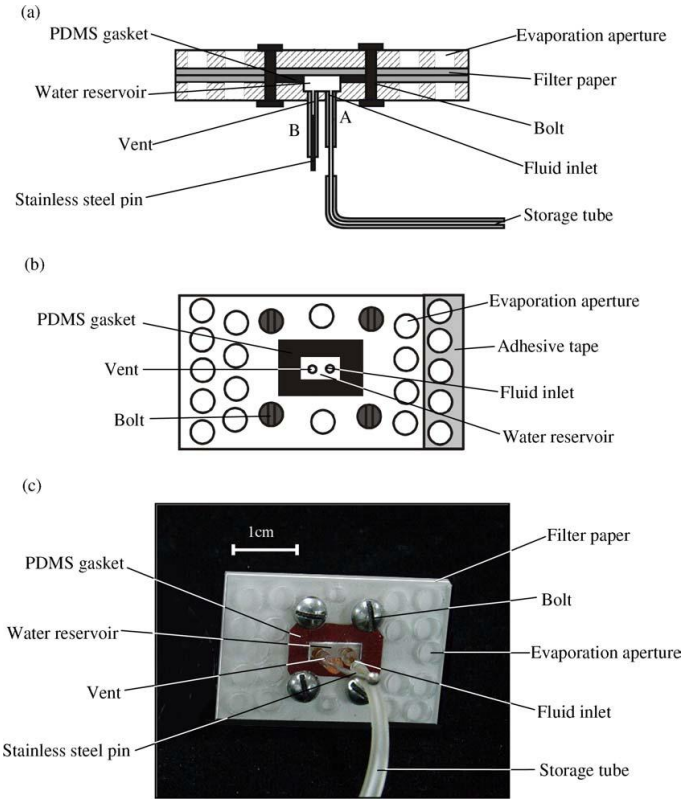

Fig 1.5: Guan et al.'s evaporative membrane micropumping system [41].

1.5 Roof Thermal Shielding

Traditionally, roofs have been made from materials (asphalt, clay, tar, etc.) with moderate to high absorption coefficients. While inexpensive and easy to install, much of the incoming solar radiation is absorbed and transferred into the structure, which must then be cooled. To mitigate the effects of direct exposure to incoming radiation, the option exists to alter the roof albedo by painting it white [44] or increasing its reflectivity [45]. Others have studied the feasibility of using evaporation systems on roofs [46-51]. In an effort to block incoming energy, some have used the phase change of a liquid to a gas to absorb incoming radiation. Several numerical studies have been performed analyzing the performance of evaporation systems on roofs. Cheikh and Bouchair [46] modeled a water filled rock bed with a white painted aluminum covering that functioned like a heat pipe and compared it to a bare roof in hot arid climates. Their dynamic model showed a relatively constant interior temperature when using the roof cooling system. Additionally,

their study showed up to an 8 °C temperature difference with and without their system on a hot July day in Algeria. When the roof cooling system was combined with nighttime ventilation, the interior temperature decreased further allowing for even lower daytime temperatures. Chen and Liu [47] thermally modeled a water gravity fed wall of a building and estimated a temperature difference between the interior and external environments of up to 8°C for an external ambient temperature of 40°C. It was also shown that when the porous plate thickness was decreased, the lower thermal capacity caused a smaller temperature difference between the interior and the ambient. Al-Turki and Zaki [48] investigated spraying a flat roof surface intermittently to determine the effect on cooling load. Their model suggested that a time-dependent-step spray was more effective than uniformly spraying. They estimated that in Jeddah, Saudi Arabia, this method could reduce cooling loads up to 40%.

Wanphen and Nagano [50] looked at several porous and non-porous (i.e., silica sand, pebbles, volcanic ash and siliceous shale) roofing options weighing their cooling capabilities on their moisture absorptance and evaporation potential. It was shown that siliceous shale, because of its large pore size, was best at absorbing water vapor of the materials tested. This is important for dehumidifying the surround environment at night thus creating water reserves for use during the day. When it came to liquid absorption, however, volcanic ash performed the best because of its high capillarity. While testing evaporation capabilities, volcanic ash also performed the highest due to its high capillary forces. It was shown that the release of latent heat increased with finer particles. On the other hand, larger particles allowed for ventilation which enhanced evaporation and exhibited lower surface temperatures. Sethi and Sharma [52] provided a review of roof cooling systems where water was dispersed in a thin layer over a roof [53-55]. Sodha, et al. [53] found that heat flux was significantly reduced when employing such techniques. Giacomelli and Roberts [54] reported that with the use of a wet, white polyester blanket on a greenhouse roof, interior temperatures were reduced 5 – 6 °C than without the wetted blanket. Mannan and Cheema [55] found similar success when watering an inclined roof from a pipe that ran the top length of the roof. While the results were

generally positive, requirements such as the need for inclined roofs, something not common in the commercial sector, the fact that water needs to be brought to the roof, which could involve the use of a pump, and the potential for under and overwatering, still need to be addressed.

1.6 Proposed Work

Transpiration inspired systems, specifically those built off of the principle of evaporation, have shown that it is capable of moving fluid passively. The available literature has presented a good basis for bio-inspired transpiration pumping on a small scale, but it often involves microfabrication. Additionally, many areas of such systems have yet to be explored, such as evaporative surface dimensions, evaporative surface characteristics, channel feeding dimensions and pumping height. Furthermore, phase change is known to be a simple method to remove large amounts of energy. With building cooling being a large contributor to energy usage, integration of evaporation to a roof has the potential to alleviate some of the cooling load. However, water dispersion methods leave something to be desired. Pumps must first bring the water to the roof while a control system would be necessary to properly disperse the water as to not under or overwater. When both passive pumping and evaporative cooling are combined together though, the potential exists for a robust, energy dissipating system.

Therefore it is the goal of this research to develop a passive pumping, evaporation based system for thermal management. This system, consisting of an evaporative surface (membrane), feeding channel and reservoir, is developed for implementation on a roof structure for the purpose of air conditioning load reduction. In the development of such a bio-inspired system, several studies were performed to understand each component of the system and their effects and limitations on operation. First, in Chapter 2, the delivery path's geometric parameters (i.e., tube diameter and length) were constrained to determine its effect on evaporation rate. In doing so, the suction pressure was also measured and equated to pumping height. In Chapter 3, the system's performance was investigated when in direct contact with a constant heat flux. Chapter 4 explored the

degradation and fouling of a membrane when subjected to pumping salt water. To conclude the experiment portion, in Chapter 5, the system's performance was tested in a real world application by shielding a model section of roof from solar thermal loading. In Chapter 6, a justification was provided for the allocation of resources consumed by the evaporation system. In the final chapter, Chapter 7, the conclusions of this investigation are present along with recommendations for future work.

Chapter 2. Characterization of Geometric Parameters

Previously, experimental work has been done to mimic the transpiration in plants [9, 10, 39-42]. In their various experimental setups, those groups were successful at moving fluid through a microfluidics network using evaporation from channels or membranes. Those setups, however, involved microfabrication, which can be costly and time consuming. Moreover, driven by their application purposes, their prototypes were small and did not lend themselves to being scaled up. Additionally, direct measurement of suction pressure in a biomimiced system could not be found in the literature.

In this study, a low-tech evaporative pumping system that does not require microfabrication was designed, constructed and tested. Commercially available micro tubing would replace the specially assembled micro channels of others' works. It was instrumented to measure evaporation rate and suction pressure while varying component configurations, i.e., membrane area and tube length and diameter. Of interest was the influence each component's geometric size had on the measured parameters.

2.1 Experimental Setup

The evaporative pumping system consisted of a porous membrane connected to a distilled water reservoir via a micro channel and tubing, Figure 2.1. The reservoir sat on a balance (Denver Instruments PI - 214, range 0 to 210 g, resolution 0.1 mg), which recorded mass loss to a spreadsheet file using Denver Instruments' proprietary software. To prevent unwanted evaporative losses from the reservoir to the atmosphere, its top was covered with a lid while a tiny pinhole maintained the reservoir pressure equal to the room pressure. Due to the slow rate of mass decrease in the reservoir, combined with the reservoir not being airtight, it was safe to assume that the interior of the reservoir was at room atmospheric pressure. Because all mass loss from the water reservoir was due to evaporation from the porous membrane, the balance was effectively recording the evaporation rate from the membrane. Due to the balance's sensitivity to air currents, it was placed in a specially designed acrylic isolation box so the balance sliding door could remain open during testing. The mass loss from the covered reservoir by itself was

confirmed to be negligible when the balance was left to record mass while no membrane evaporation was occurring. The mass rate decrease was found to be less than 1% of the lowest evaporation rate that would be tested as a result of the experimental setup configurations.

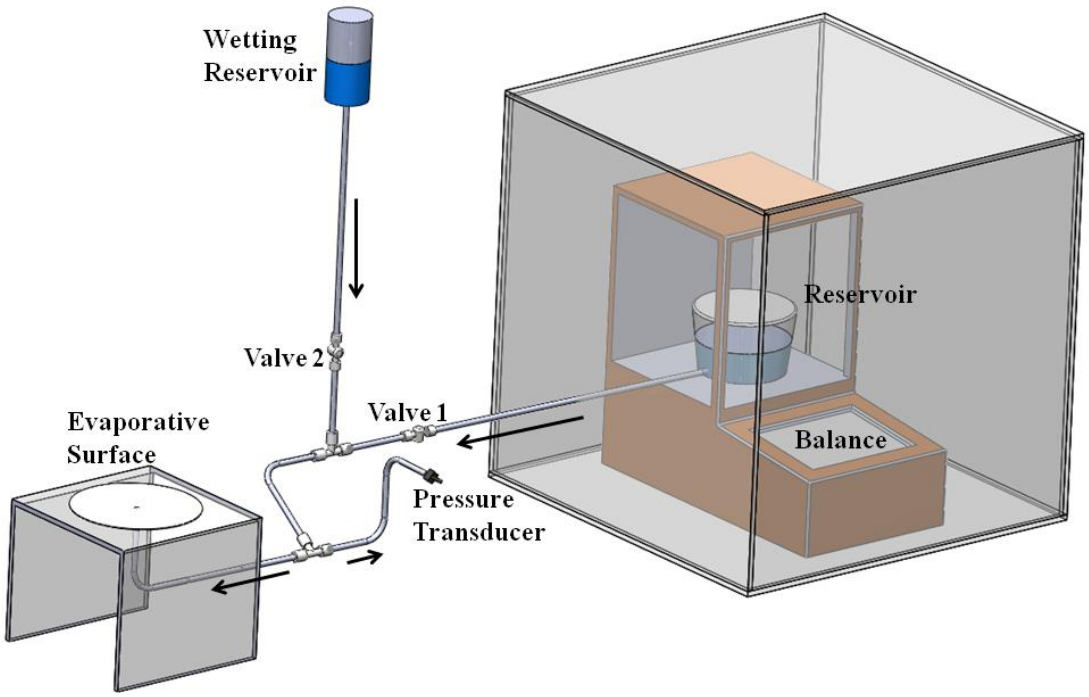

Fig. 2.1 Experimental evaporative pumping system setup.

To serve as micro channels to irrigate the membrane, high-pressure polyetheretherketone (PEEK) tubing were selected. The PEEK tubing fit snuggly into a small perpendicular hole in the center of an acrylic plate that served as a substrate to support the membrane. The outlet of the PEEK tubing was flush with the top surface of the acrylic substrate while sealant was applied to the underside of the acrylic where the tube entered to prevent leakage. Three values of channel diameter, length, and membrane area could be interchanged: (i) diameters of 127.0, 177.8, and 254.0 μm, (ii) lengths of 2.54, 7.62, and 15.24 cm, and (iii) areas of 20.3, 81.1 and 176.7 cm^2 (before wetting). Additional tubing, $1/8^{th}$ inch ID Tygon tubing, was used to connect the micro channel to the reservoir. All tubing was purged of air bubbles to ensure single phase flow. The

system also featured Swagelok valves for turning the system on and off – the operation procedure will be discussed later. A parallel study showed that any pressure drop in the Tygon tubing and connectors was negligible compared to the pressure drop in the micro channel and did not affect the system. Additionally, any capillary rise of the fluid in the Tygon tubing was negligible.

Two additional lines were split from the main supply line. One line connected to a ± 34.5 kPa differential pressure sensor (Omega PX26-005DV, calibrated uncertainty was 0.017 kPa at 95% confidence) with one side open to atmosphere. A complete analysis regarding the pressure transducer's calibration and uncertainty can be found in Appendix B. Pressure was calculated using the density of water at atmospheric pressure and a temperature of 23.5°C. The other line connected to another reservoir placed high above the channel. The purpose of this second reservoir was for initially wetting the membrane to start the system. It too featured an on/off valve.

2.2 Membrane Characterization

The evaporative surface was a thin porous membrane (Fisherbrand Glass Fiber Filter Circles G6). The microstructure was examined using a Jeol JSM-5610 scanning electron microscope (SEM). The structure was of a random nature with much interlocking between fibers, Figure 2.2. The fibers were relatively smooth, constant diameter rods ranging in diameter up to ~3 μm, however, the fiber length could not be identified. Spacing between fibers was estimated to be up to 7 μm. The size of the fibers and spacing between fibers plays a major role in the capillary spreading of a fluid in the membrane.

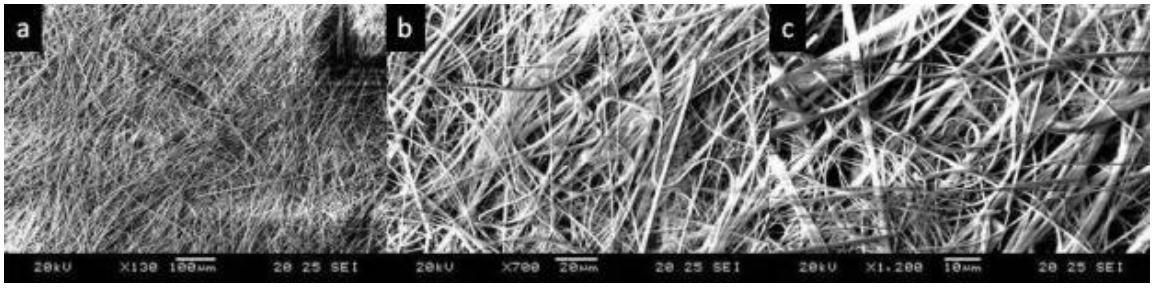

Fig. 2.2 SEM images showing the structure of the porous membrane evaporative surface.

2.3 Experimental Procedure

To begin the experiment, the desired channel diameter and length and membrane area were selected. A dry membrane was placed on the acrylic substrate and centered on the outlet of the PEEK channel. The height of the reservoir's free surface was brought to just below the height of the membrane. Valve 1 (see Figure 2.1) was closed and valve 2 was opened to begin the "forced" wetting process of the membrane. The aid of gravity was used in the initial wetting of the membrane because this study investigated the steady state flow rather than the initial wetting phenomena. Once the entire membrane was visually confirmed to be wet, valve 2 was closed and valve 1 was immediately opened to begin the evaporative pumping process. The balance recorded measurements of the mass loss from the reservoir every minute to a spreadsheet file. In the event that the membrane was initially overwatered, the system would self-regulate, i.e. wait until excess water had evaporated from the membrane before drawing replenishment from the reservoir. Conversely, if the membrane was initially under watered, an initial period of high evaporation rates were measured until the membrane reached its steady state wetness. Temperature and humidity of the room were recorded using a Fisher Scientific Fisherbrand traceable Hygrometer/Thermometer. While these two factors were not controlled during the tests, over the course of all experiments, the temperature of the room remained at 23.5 ± 0.5°C while the humidity was 45% ± 10%. During any particular trial, however, because of the short duration of a test, the temperature and humidity remained relatively constant. It is important to note that humidity is indeed a

relevant factor when determining evaporation rates; however, this preliminary study only focused on the parametric effect of the three variables previously discussed.

Steady state operation of the system was determined by a constant evaporation rate for at least 30 minutes. Upon reaching steady state, the reservoir was disconnected by closing valve 1. This left the evaporative surface only in contact with the pressure transducer. Over the course of up to two hours following the closing of valve 1, increasingly negative pressures were recorded as the evaporative surface dried out. The experiment was considered finished when the suction pressure returned to roughly a zero pressure differential, which corresponded to the column of water breaking from the membrane.

A minimum of three experiments were performed under the same conditions. A new membrane was used for each test. It was found that rewetted membranes (membranes that were tested, dried out and then wetted again) produced evaporate rates that were lower than new membranes. While membrane degradation was not the focus of this part of the investigation, this factor was eliminated for the investigation. It would later be determined that the membrane was indeed deteriorating over extended periods of operation, but that will be discussed in a later study.

2.4 Experimental Results

Representative results are shown in Figure 2.3 for steady state conditions of channels 254.0 μm in diameter and 2.54 cm in length with evaporative surface membrane diameters of 5.08, 10.16, and 15.00 cm. Between trials, the results were repeatable with an evaporation rate of approximately 3.7, 12.3, and 22.3 mg/min, respectively.

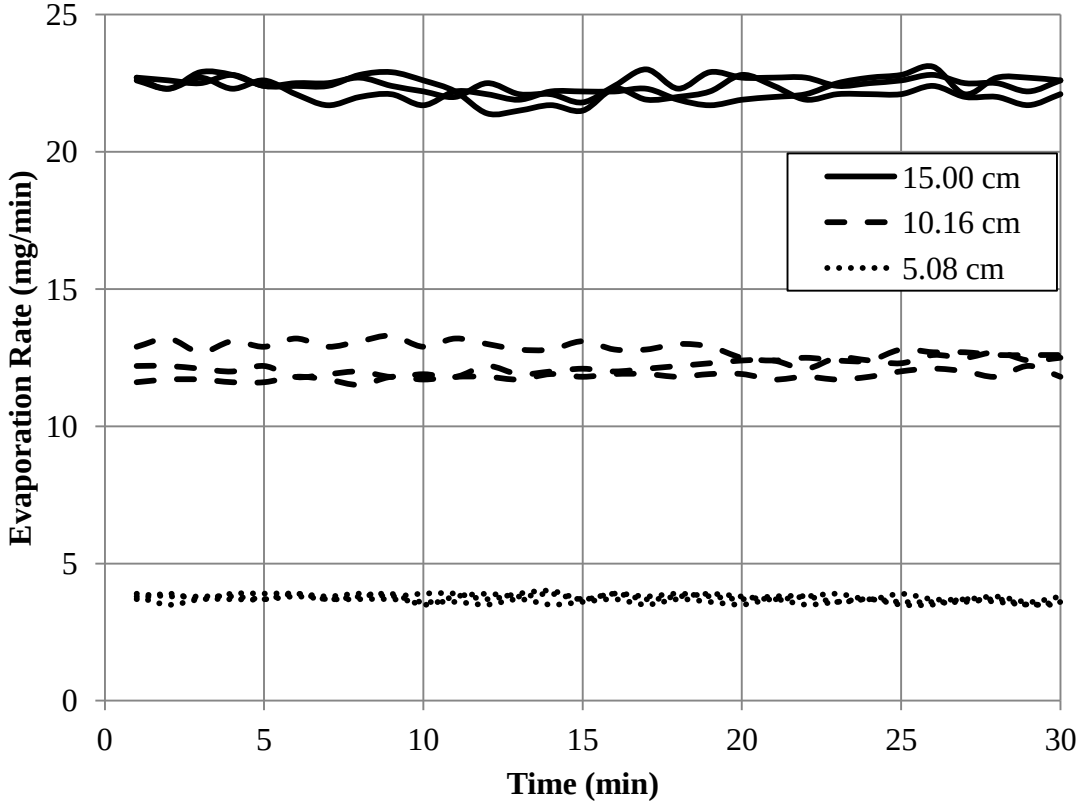

Fig. 2.3 Typical data collection of mass evaporation rate showing repeatability between trials. Parameters: 254.0 μm channel diameter, 2.54 cm channel length, and surface diameters of 5.08, 10.16, and 15.00 cm.

Additionally, the suction capability of the evaporative membrane was measured as a function of the tubing diameter. Typical trials are presented in Figure 2.4 for all three micro channels tested (i.e., diameters of 127.0, 177.8, and 254.0 μm) at a length of 2.54 cm and a membrane diameter of 15.00 cm. The results showed that there was no significant effect on the evaporation rate, however, increasing the tube diameter did increase the maximum attainable suction pressure. Also, it can be observed, for all cases, that the suction pressure immediately began increasing when the membrane was disconnected from the water reservoir, and that the suction rate increased as the tubing diameter decreased. Furthermore, Figure 2.4 shows that all tests experienced a period of constant suction rate increase followed by a sharp increase in pressure. As membrane dry

out occurred, evaporation caused a volume reduction of water in the rigid space that was the membrane/water column assembly. This volume reduction generated a tensile stress which was registered by the pressure transducer. The suction pressure increased until it reached the capillary pressure at which time, the seal between the membrane and tubing broke, causing air to rush in, returning the water in the tubing to atmospheric pressure. The capillary pressure can be found using the Laplace-Young equation, $P_c = 2\gamma \cos\theta / r$, where γ is the surface tension, θ is the contact angle of water and r is the radius of the pore. For the pore radius of the membrane, the capillary pressure was roughly 35 kPa. This corresponded to the maximum pressure reached for the tubing with the lowest pressure drop. One possible explanation for the effect of the tubing diameter on the suction rate and the maximum suction pressure had to do with the fact that, as the tubing diameter decreased, it had to overcome larger hydrodynamic resistive forces. This led to the thought that if the evaporative surface was raised above the reservoir, larger diameter tubing would allow for greater height differences with smaller performance impacts when passive pumping was employed. Finally, the pumping height was determined by dividing the suction pressure by gravity and the density of the fluid, $H = P/\rho g$. For example, with a suction pressure of -30 kPa, which was close to the maximum suction pressure for the tubing with a diameter of 254 μm, the system should pump to roughly 3.0 meters.

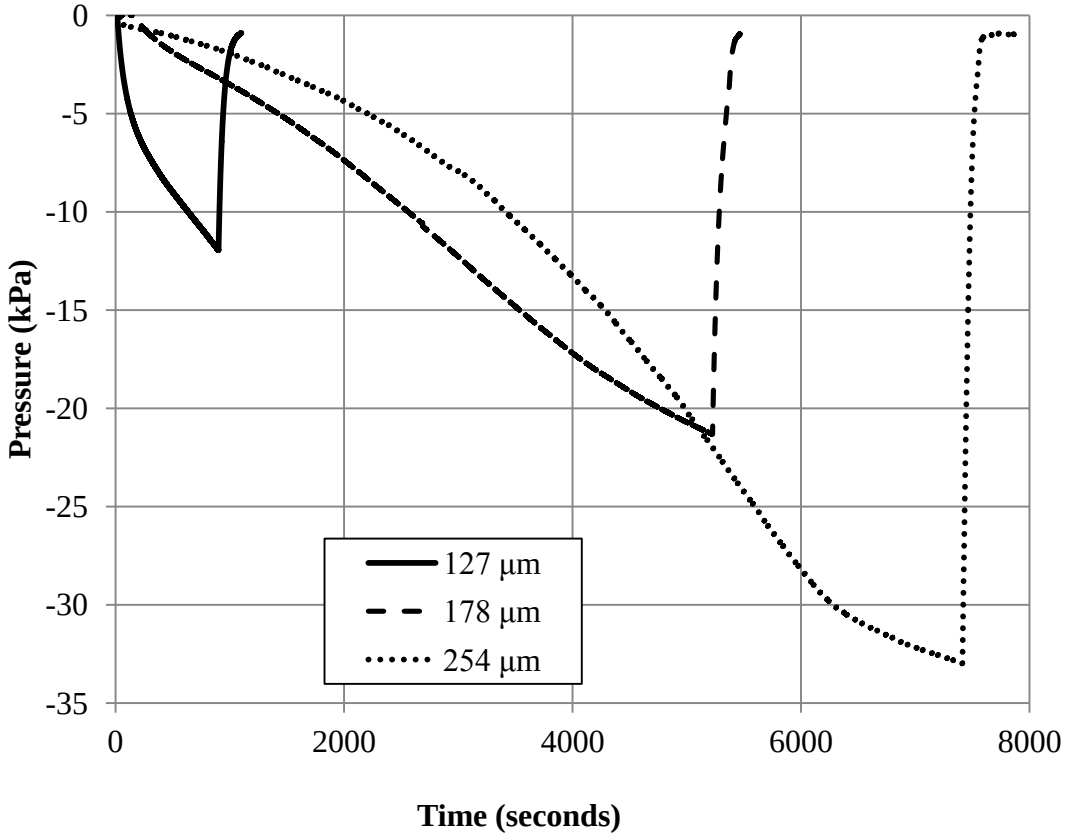

Fig. 2.4 Typical suction pressures as the membrane dries out for varying micro channel diameters. Parameters: channel length of 2.54 cm and membrane diameter of 15.00 cm.

The next parameter to be investigated was the tube length. Tests were performed using tubing of varying lengths with diameters of 254.0 µm and evaporative membrane diameters of 15.00 cm. Again, the tube length did not affect the evaporation rate for the dimensions tested. However, its effect was observable in the suction pressure that could be obtained, Figure 2.5. Larger suction pressures were reached with shorter lengths, possibly for the same hydrodynamic reasoning as why channel diameter affected pressure. At increasing lengths, the height difference between the evaporative surface and the reservoir would detrimentally impact the system's performance. Also, it is expected that at some length, the system would not be able to overcome the pressure drop in the tubing and pumping would cease.

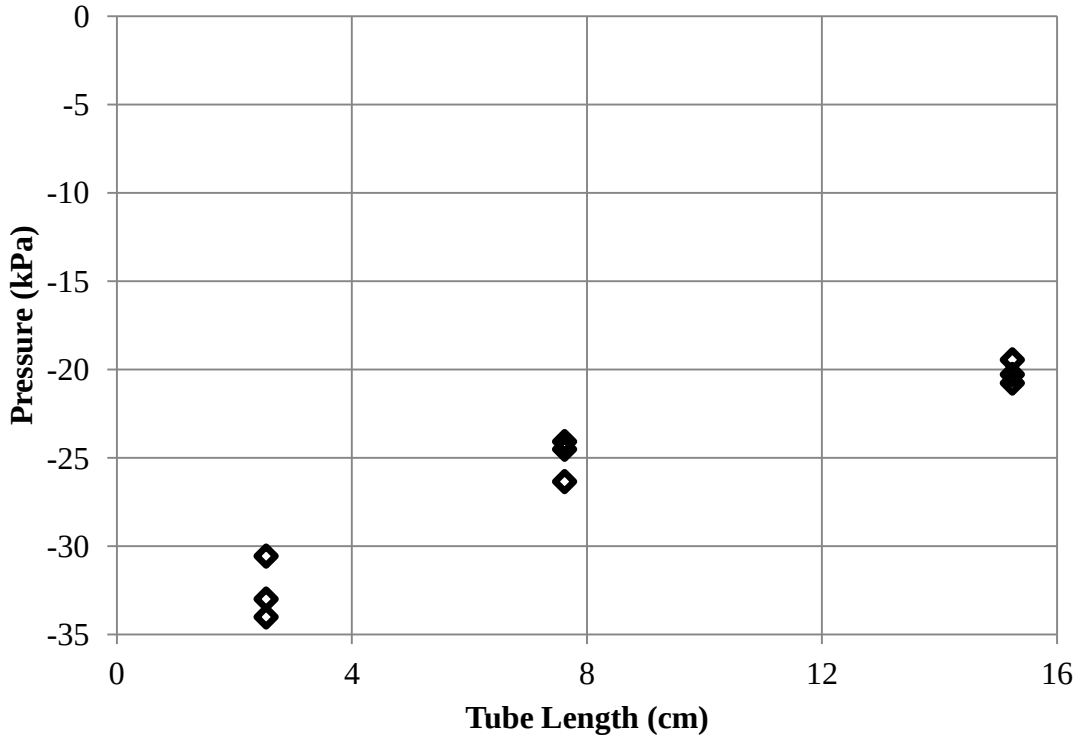

Fig. 2.5 Effect of the micro channel length on the suction pressure. Parameters: 254.0 μm channel diameter, 15.00 cm membrane diameter.

Lastly, the evaporative surface diameter was varied. The suction pressure remained unaffected with varying surface diameter (areas). This suggested that the suction pressure was governed mostly by the micro channel parameters and micro channel/membrane connection. On the other hand, the evaporation rate increased with evaporative surface area, as shown in Figure 2.6 as square markers. As expected, the relationship was nonlinear with increases in surface diameter yielding diminishing increases in evaporation rate. This was more obvious when the average evaporation rate was normalized over surface area, Figure 2.6 as circular markers. Increasing surface areas led to lower evaporation rates per unit area. This was because not enough fluid was present to saturate the outer regions due to evaporative losses at preceding radii. In a system fed by a point source, like the one discussed in this dissertation, fluid transported in the radial direction would be completely evaporated at a certain radius. For this

system, following the trend of the normalized evaporation rate, it was estimated that the critical radius was roughly 20 cm, as the membrane material at a radius greater than this critical radius would most likely not receive fluid. It is expected that the interface between wetted and non-wetted areas within a membrane would move depending on membrane properties such as permeability and porosity. The normalized evaporation rate with respect to the membrane radius is an important aspect when considering application purposes, such as the one discussed later, because an array of point sources would be needed for scaling the system to larger areas. Spacing of the point sources is critical to maintain high evaporation rates over the whole surface area thus not limiting the system's cooling capabilities.

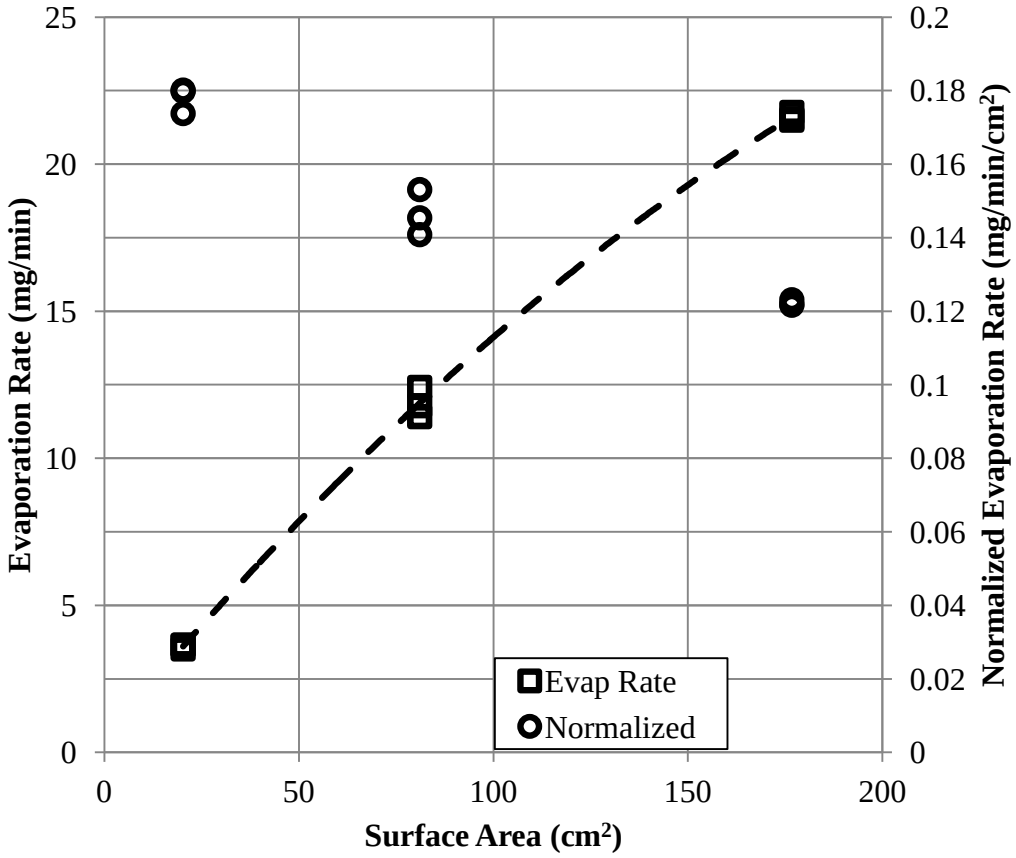

Fig. 2.6 Effect of the membrane diameter on the absolute and normalized evaporation rates. Parameters: 254.0 μm channel diameter, 2.54 cm channel length.

Chapter 3. Evaporative Cooling of an Internally Heated Surface

The phase change of a substance has the capacity to absorb large amounts of energy. For example, the human body uses sweat evaporation to help with cooling. The concept is currently utilized in the electronics industry through spray cooling. Additionally, phase change is under development for use in building design where thin films of water run down the roofs of buildings [53-55].

In this study the evaporative, passive pumping system of the previous study, §2, was retrofitted to be applied to the surface of a heater, which provided a constant heat flux. A similar testing technique was used where both evaporation rate and suction pressure were measured for different test parameters, i.e., heat power and membrane area. Furthermore, the operating temperature of the heater was monitored. The tests aimed to determine the ability of the evaporation system to lower the body temperatures of a heat flux source as compared to natural convection cooling.

3.1 Experimental Setup

The evaporative cooling system, Figure 3.1, was constructed from a porous membrane serving as the evaporative surface, which sat on a circular copper plate. On the underside of the copper plate, heaters were attached for the purpose of providing a constant heat flux. Through the radial center of the plate, tubing connected the porous membrane to a water reservoir and pressure transducer. The water reservoir sat on a balance, which recorded mass loss over time representing the mass that was evaporated.

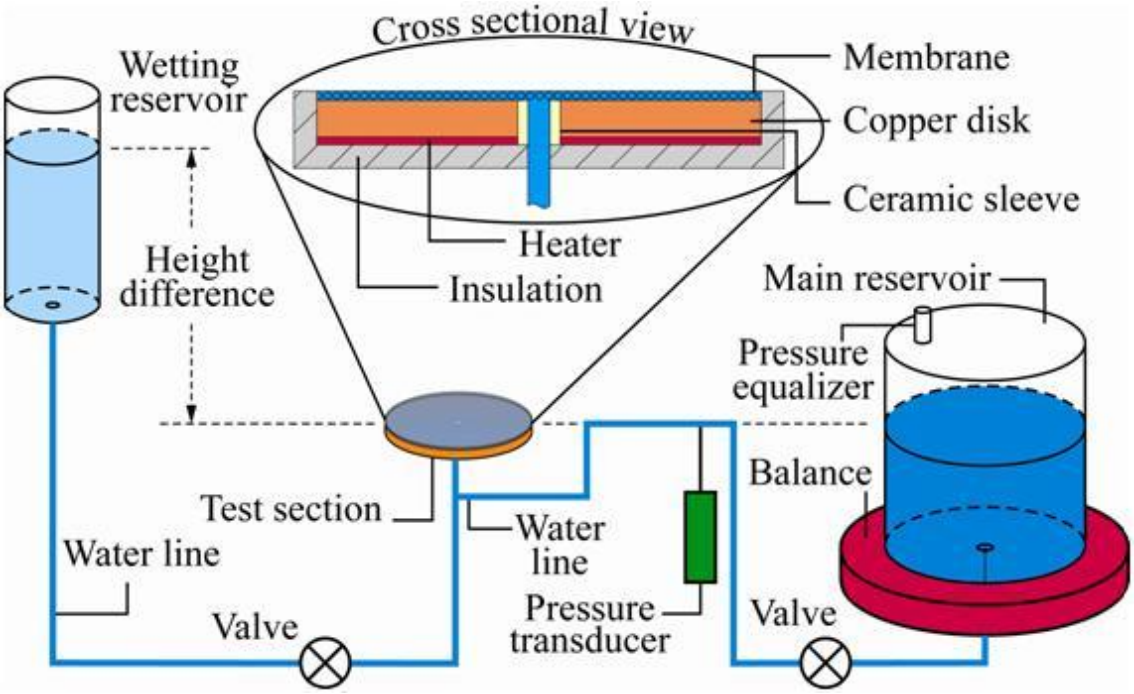

Fig. 3.1 Evaporative pumping system with heater.

The copper (alloy 110) plate measured 15.24 cm in diameter (surface area of 182.4 cm^2) and 1.12 cm thick. Ultra-thin polyimide film heaters were placed on the bottom side of the plate. The heaters were 28 volt AC and had a max power density of 0.78 W/cm^2. A total of 129.0 cm^2 of the 182.4 cm^2 was covered with the heaters which were connected in parallel. The power supplied to the film heaters would range from 0 to 4.5 W. Due to the thermal properties of the copper alloy, the plate was assumed isothermal and experimentally confirmed which will be detailed later. A complete analysis regarding the isothermal assumption can be found in Appendix E. Insulation (alumina silica ceramic insulation) was placed underneath and around the sides of the plate forcing all heat flow through the top of the plate where the membrane sat. A complete analysis regarding the heat loss thermal assumptions can be found in Appendix F. To monitor the temperature in the plate, three type K thermocouples were placed at the plate's mid plane at radial distances of 2.54, 5.08, and 7.62 cm (highest calibrated

uncertainty of the thermocouples was 0.11 °C at 95% confidence) A complete analysis regarding the thermocouples' calibration and uncertainty can be found in Appendix A..

Flush with the top of the copper plate and through its radial center, Tygon tubing ($1/8^{th}$ inch ID) connected the porous membrane (Fisherbrand Glass Fiber Filter Circles G6) to the water reservoir. This was the same membrane type as used in the previous study, §2. Three different membrane surface areas were used for testing, i.e., 20.3, 81.1 and 176.7 cm^2 corresponding to diameters of 5.08, 10.16 and 15 cm, respectively. For tests using membranes smaller than the plate diameter, insulation was also placed over any exposed parts of the plate. A ceramic sleeve was wrapped around the tubing while it was in the heater to minimize heat transfer into the water. To ensure single phase flow, air bubbles in the system were flushed out.

From the main line between the balance and the porous membrane, two addition lines were teed off. One line connected the system to a ± 206.85 kPa differential pressure sensor (Omega PX26-030DV, calibrated uncertainty was 0.032 kPa at 95% confidence) with the sensor's other side open to atmosphere. A complete analysis regarding the pressure transducer's calibration and uncertainty can be found in Appendix B. The center of the pressure transducer was at the same height as the evaporative surface for an initial 0 differential pressure. The other line connected the system to an additional reservoir located high above the setup. The purpose of this reservoir was only for initial wetting of the membrane and was closed during experimentation.

3.2 Experimental Procedure

The experimental procedure was similar to that of the previous study, §2. The same method was used for initially wetting the membrane, recording mass loss, and measuring suction pressure. For this objective, a range of fluxes were chosen to supply to the plate heaters for parametric testing by varying the power input, 0 to 4.5 W. In addition to mass loss, temperatures in the plate were recorded 5 times a second over the course of the experiment to a separate spreadsheet file using NI Labview.

3.3 Experimental Results

The results of the parametric analysis of the passive evaporative pumping system for the purpose of heat removal are presented next. The evaporation rate trends resembled those discussed in the previous study, Figure 2.3. Between trials of different powers supplied to the heater, a constant evaporation rate was observed. With the supplied power at various loads between 0 and 4.5 W, using a 15 cm diameter membrane, the evaporation rate was linear, Figure 3.2. An increase in power caused the evaporation rate from the membrane to increase.

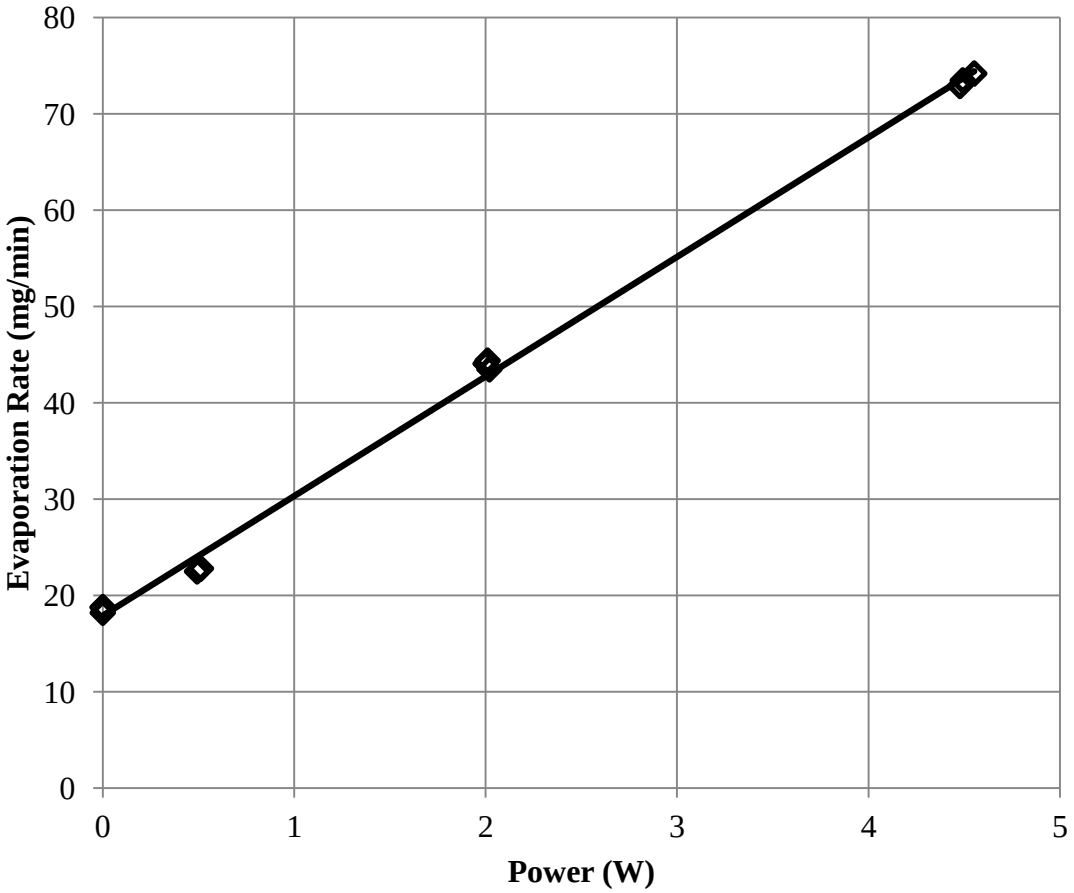

Fig. 3.2: Evaporation rate verse power supplied for a surface diameter of 15 cm.

Like the evaporation rate, at steady state, the temperature of the heater was also steady. From the three thermocouples that had been placed in the mid-plane of the plate moving radially outward, no gradients were seen thus confirming the isothermal nature of the copper alloy. With increasing amounts of power supplied to the heater using a 15 cm diameter membrane, the temperature increased. Additionally the average evaporation rate increased with the heater temperature, Figure 3.3. Similar trends are expected for different sized membranes. Because the energy goes towards evaporating the water, the heater was maintained at a lower temperature than had the heater relied strictly on natural convection dissipating heat. With the heater powered at 0.5 W and no cooling assistance provided beyond natural convection, the heater temperature was measured to be 27.4°C, 3.6°C above room temperature and 7.0°C above the evaporative assisted heater temperature, leading to a calculated heat transfer coefficient of 7.5 $W/m^2/K$. Considering the case where 2.0 W were supplied to the heater and the evaporative system maintained the heater at 24.7°C, a heat sink of at least 2963 cm^2 exposed to natural convection would have been needed to duplicate the temperature of the 182 cm^2 evaporative surface.

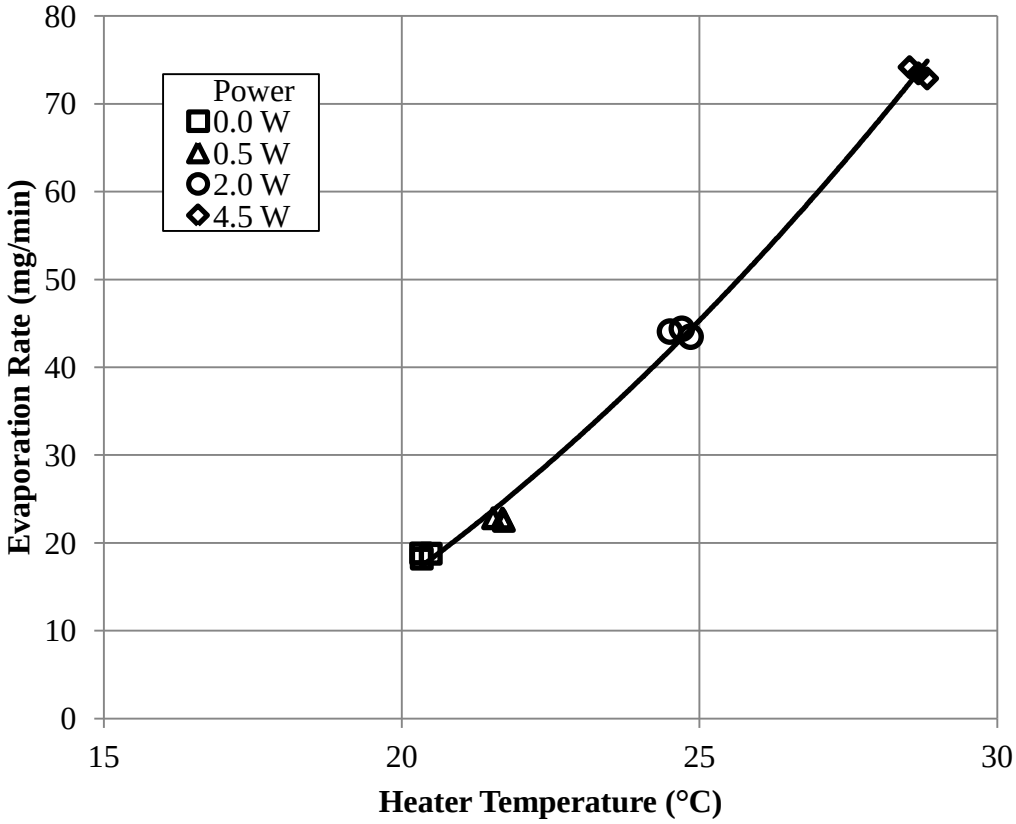

Fig. 3.3: Evaporation rate versus temperature of plate for a membrane surface diameter of 15 cm.

As smaller evaporative surface areas were used, insulation was placed around the exposed parts of the heater forcing all heat flow through the evaporative surface. With the power held steady at 4.5 W, as surface area decreased, evaporation rates decreased as well, Figure 3.4 circular markers. However, for the same power, when considering the normalized evaporation rate per unit area, decreasing surface areas saw higher normalized evaporation rates, Figure 3.4 square makers. This led to the belief that with increased distance from the point source, the "drier" the membrane. While fluid was reaching further radii, not enough fluid was reaching those sections for them to be considered saturated due to evaporative losses at previous radii. At some critical radius, the membrane would receive no fluid and would be dry. It can be seen that the trend of

the evaporation rate was beginning to level off with the 15 cm diameter membrane suggesting that the critical membrane size was approaching.

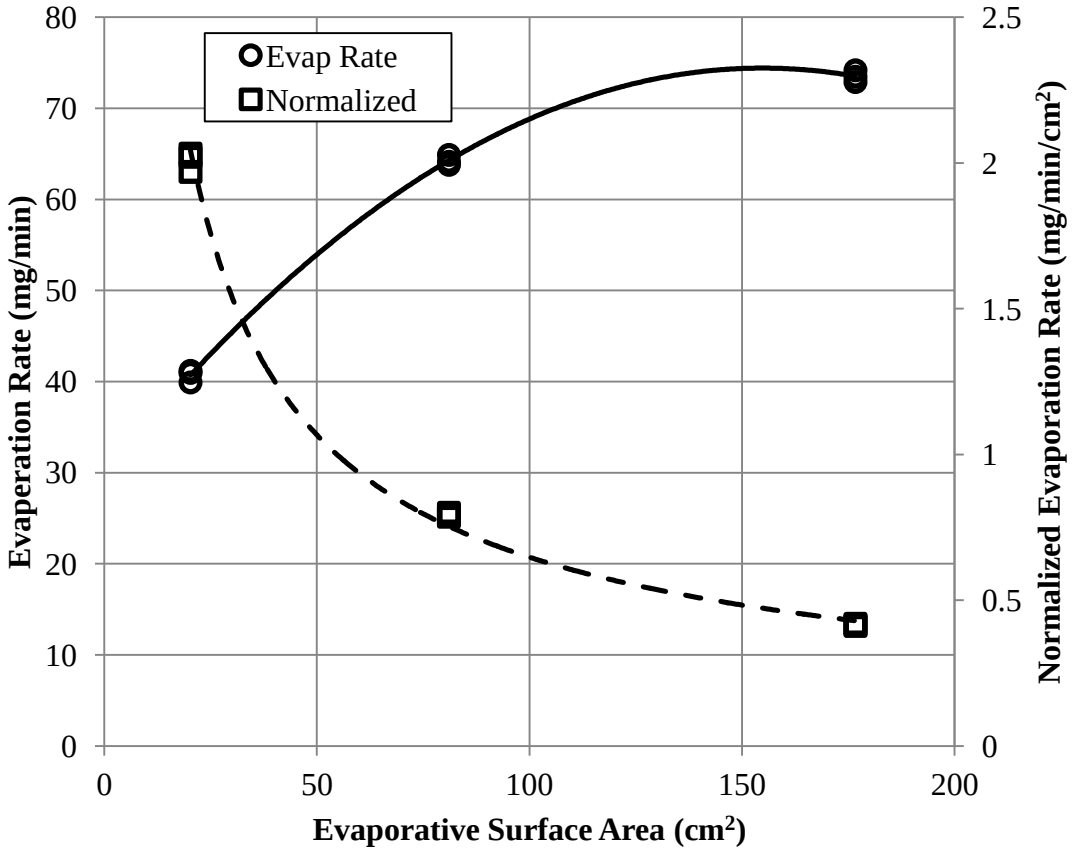

Fig. 3.4: Evaporation rates and normalized evaporation rates verse membrane surface area for 4.5 W supplied to the heater.

With the decrease in evaporation rates from the smaller membranes, the steady state temperature of the heater increased for a constant power of 4.5 W, Figure 3.5 (left axis). At the same time, as the temperature of the heater increased because of the imposed restriction on evaporation area, the system was demonstrated to be able to dissipate increasingly higher heat fluxes. Recall that for membranes smaller than the copper surface, insulation was placed around exposed areas forcing heat flow through the

membrane. The system was able to maintain the heater temperature at a relatively cool 43°C while dissipating 2250 W/m^2.

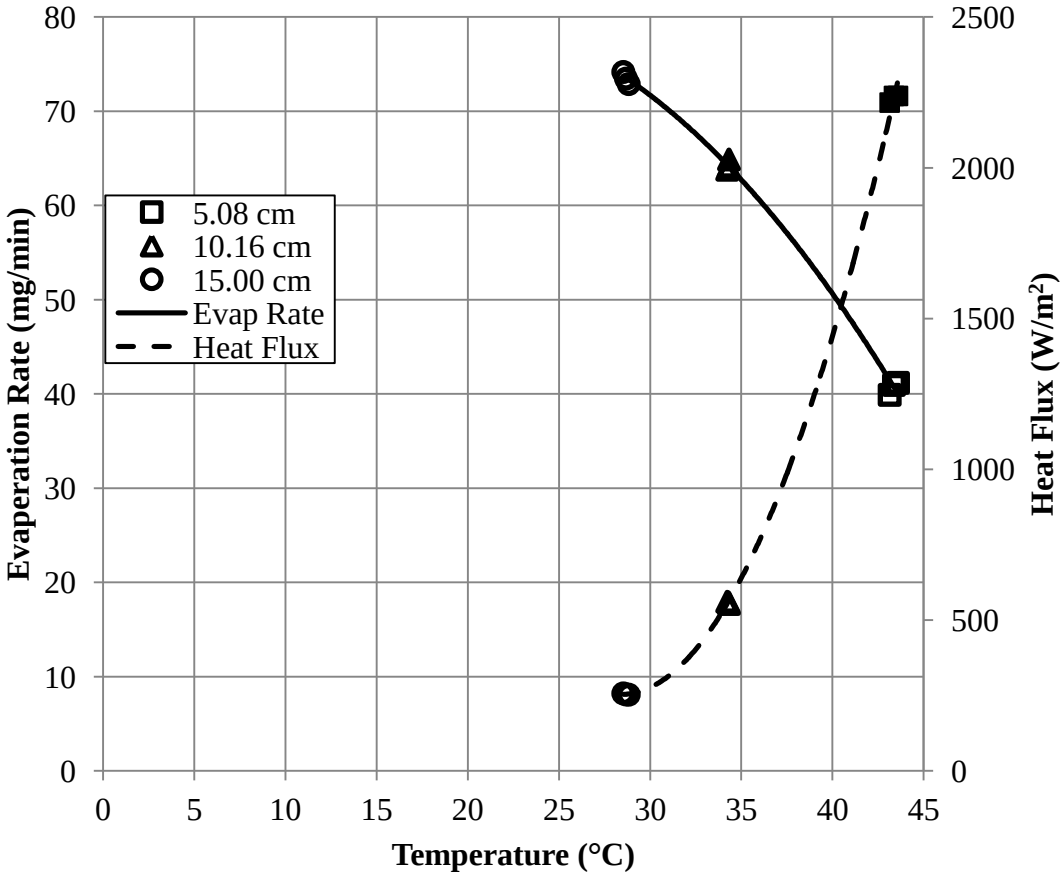

Fig. 3.5: (left axis) Evaporation rates as a function of the heater temperature for various membrane diameters for a heater power of 4.5 W. (right axis) Temperature of the heater with varying evaporative surface diameters.

Lastly, the suction pressure was measured when the system was at steady state and the membrane, measuring 15 cm in diameter, was disconnected from the reservoir resulting in the membrane drying out. It was found that suction pressure was not determined by the heater temperature, Figure 3.6. The higher temperatures did, however, cause the membrane to dry out quicker causing the suction pressure peak to be reached

faster. Additional membrane sizes were not tested because of the findings in the previous study that suggested membrane size did not affect suction pressure, §2.

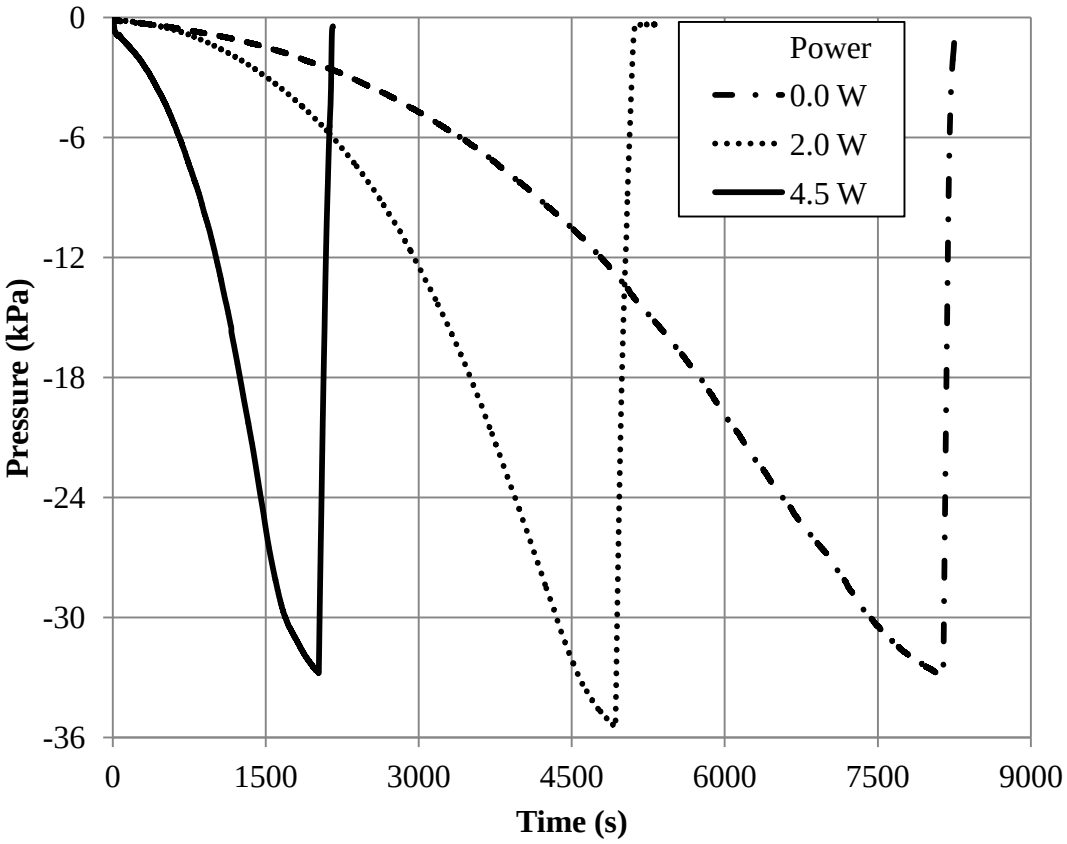

Fig. 3.6: Suction pressure as 15 cm diameter membranes dried for various heater powers.

Chapter 4. Membrane Degradation Study

This study is made clearer when considering its use in conjunction with the last experimental study, §5. The applications of the system described in this dissertation would be implemented in environments that present conditions far less ideal than in laboratory testing. In laboratory tests for studies 1 and 2, §2 and §3, the working fluid had been distilled water in a relatively clean air environment. When implemented in the field, it is impractical to think that distilled water would be available and the membrane would not be exposed air particulates not present in the laboratory. For example, a realistic design of using the evaporative system for thermal management of a building could take a sustainable approach and use reclaimed rainwater or greywater for the working fluid. The possibility arises that particulates in the water would deposit themselves in the evaporative surface, thus affecting evaporation. Furthermore, in extended periods of operation, the solid phase integrity of the porous membrane must be maintained so that the water can maintain its capillary connection.

With particulate buildup on or in the membrane, known as fouling, the porosity and permeability of the membrane would decrease thus affecting flow rate as described by Darcy's Law [23]. It is the purpose of this study to identify how evaporation rate decreases as the evaporative membrane degrades. Additionally, a proper solid phase structure will be identified for sustained operations. In this study, the evaporative, passive pumping system of the first study, §2, was retrofitted to accommodate both a distilled water and saltwater reservoir. A similar testing technique was used where evaporation rate was measured for a constant membrane area and salt to water concentration.

4.1 Experimental Setup

To test the long term structural integrity and fouling of the membrane, the same setup could be used. In both situations, the membrane sat on an acrylic substrate. Flush with the top of the acrylic surface, corresponding with the underside of the membrane, $1/8^{th}$ inch ID Tygon tubing connected to several reservoirs, i.e., main reservoir, secondary reservoir, and high water reservoir. The main reservoir sat on a balance (Denver

Instruments PI - 214, range 0 to 210 g, resolution 0.1 mg), which recorded mass loss to a spreadsheet file using Denver Instruments' proprietary software much like the setup of the first study, §2. Again, because of the sensitivity of this balance, it was contained in a specially build chamber. The secondary reservoir resided on a balance (Ohaus Scout Pro SPE602, range 0 to 600 g, resolution 10 mg) which required mass loss to be recorded manually. To prevent unwanted evaporative losses from both of these reservoirs to the atmosphere, the tops were covered with a lid while a tiny pinhole maintained the reservoirs pressure equal to the room pressure. Because all mass loss from the reservoirs was due to evaporation from the porous membrane, the balances were effectively recording the evaporation rate from the membrane. The high water reservoir was connected to the line running between the membrane and secondary reservoir. This reservoir would only be used in initial wetting of the membrane thus covering or recording reservoir levels was not important. Valves allowed for operational control of all the reservoirs to turn them on and off as desired. Additionally, air was purged from the system to ensure single phase flow.

Due to the findings during this study, two different membrane types would be used. While the reason for this will be detailed below, the first membrane was Fisherbrand's Glass Fiber Filter Circles, the same used in all previous studies, and the second membrane type was Millipore's Durapore polyvinylidene fluoride (PVDF) membrane with a porosity of 0.7, diameter of 9 cm, and thickness of 135 μm.

4.2 Experimental Procedure

To study the structural integrity of the membrane over time, an evaporation test was performed for an extended period of time, i.e., up to 1 week. This was considerably longer than any previous experiment length which typically lasted no more than 2 hours. To begin, a 9 cm diameter membrane was placed on the acrylic substrate with its center over the feeding tube. With the main reservoir containing distilled water, its free surface was brought to just below the height of the membrane. During this part of the degradation study, the secondary reservoir was not used. To begin the test, the high water reservoir

was opened, allowing for the membrane to become saturated. Upon wetted, the high reservoir was turned off and the main reservoir was opened. The balance recorded measurements of the mass loss from the reservoir every minute to a spreadsheet file.

To intentionally foul the membrane, saltwater was used in the main reservoir at a concentration of 25 grams per 100 mL of distilled water while pure distilled water was used in the secondary reservoir. A similar startup procedure was used as before concerning the membrane placement and high reservoir usage. However, upon saturation, the secondary reservoir was turned on rather than the main reservoir. The secondary reservoir was used to ensure that the membrane was at a steady state evaporation rate before switching over to the main reservoir which contained saltwater so that the experiment could proceed. Once switching from the secondary to the main reservoir, the membrane pumped salt water before becoming clogged. Time lapsed pictures taken with a camera showed the buildup of salt in the membrane as discussed in the next section. For the secondary reservoir, mass loss was recorded manually every 10 minutes. Due to the sensitivity of this balance being less than the main reservoir balance, 10 mg compared to 0.1 mg, and the sensitivity being on the same order of magnitude as the evaporation rate, ~10 mg/min, at least 4 hours were used to ensure steady state conditions. The mass loss was recorded and averaged over that time to make sure it coincided with the known evaporation rate.

4.3 Membrane Integrity Results

Initially, the Fisherbrand Glass Fiber Filter Circles were to be used throughout this entire investigation. When considering the salt buildup in the membrane discussed in the next section, it was deemed important to have an extended baseline trial of evaporation. While conducting this extended test, interesting results were obtained that showed an unexpected crash in the evaporation rate at an unpredictable time in the trial as seen in Figure 4.1. When the extended trial was done for the PVDP membrane, the crash was not observed. It should be noted that the minor peaks and troughs in the evaporation rate were related to the temperature and humidity in the environment. Due to the

extended periods of trial times as compared to before, when the test was left over night, environmental conditions changed enough to cause larger fluctuations in the evaporation rate than previously observed. The larger peaks, i.e., glass fiber around hour 84 and PVDF around hour 108, we attributed to weather fronts entering the area and confirmed at the time with publicly available weather data.

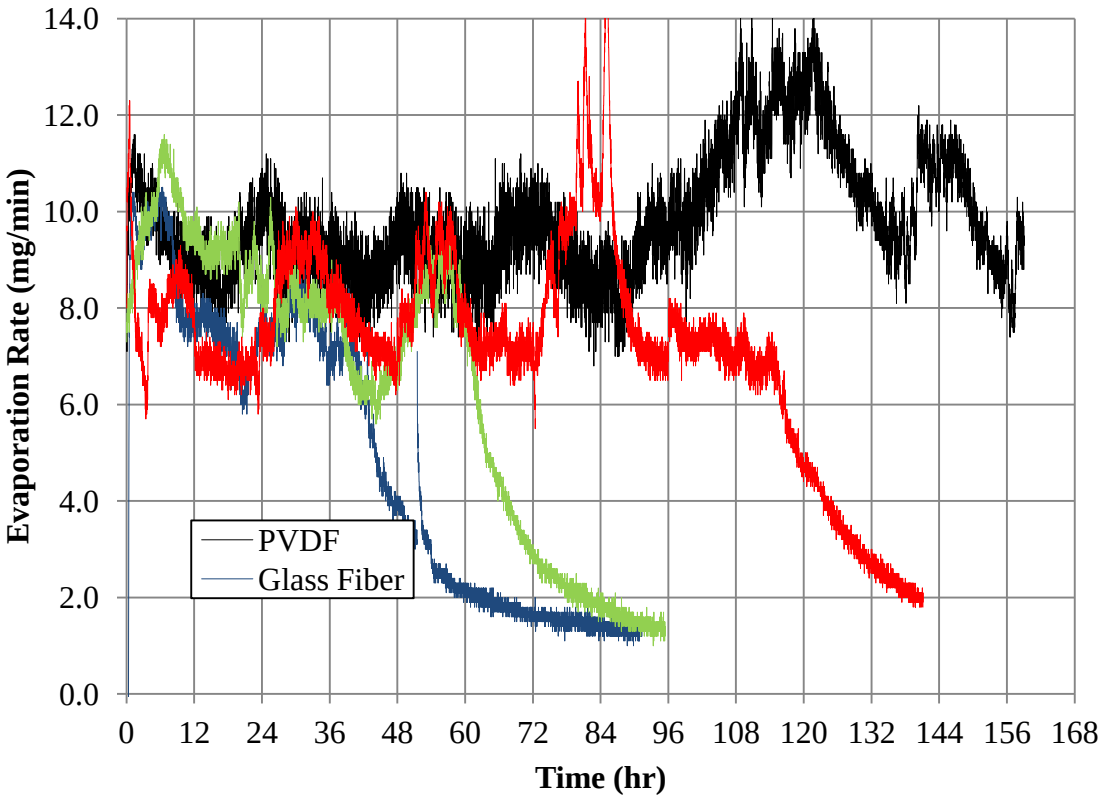

Fig. 4.1: Evaporation rate for extended time trials for PVDF and glass fiber membranes.

The cause of the random, rapid decline in the evaporation rate for the glass fiber membrane was perplexing until the membrane was viewed under a scanning electron microscope, Jeol JSM-561 SEM, following a test and after the membrane dried. Compared to a new glass fiber membrane, glass fiber membranes after extended periods of evaporation exhibited a large decrease in fiber density as seen in Figure 4.2, tiles A

verse B and C. It was hypothesized that the fibers were being carried with the flow, away from the center. Additionally, around the outer ring of the membrane, a thin white film appeared which turned out to be fibers that were carried there by the flow. Comparing locations within a post test membrane, it was seen that the closer one was to the point source, the lower the fiber density, Figure 4.2, tiles B and C. This was attributed to high local velocities near the center of the membrane as compared to further radii.

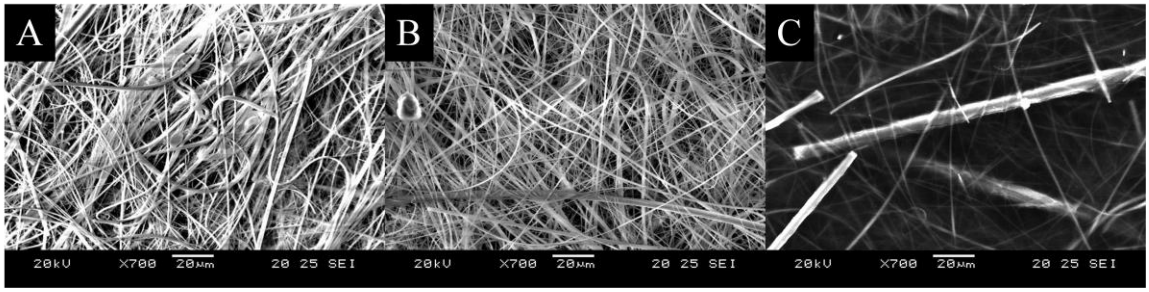

Fig. 4.2: SEM images showing the glass fiber membrane (a) new, (b) post evaporation, half radius and (c) post evaporation, radial center, all at 700x.

Because of the washout effect, it was determined that a loose fiber material could not be used for extended operations. A rigid porous matrix would not experience this washout effect thus the PVDF membrane was chosen and used for the remainder of the investigation. The pore structure was of a random nature with a manufacturer specified pore size of 0.65 μm - scanning electron microscope (SEM) images showed that the pore size reached up to 3 μm, Figure 4.3.

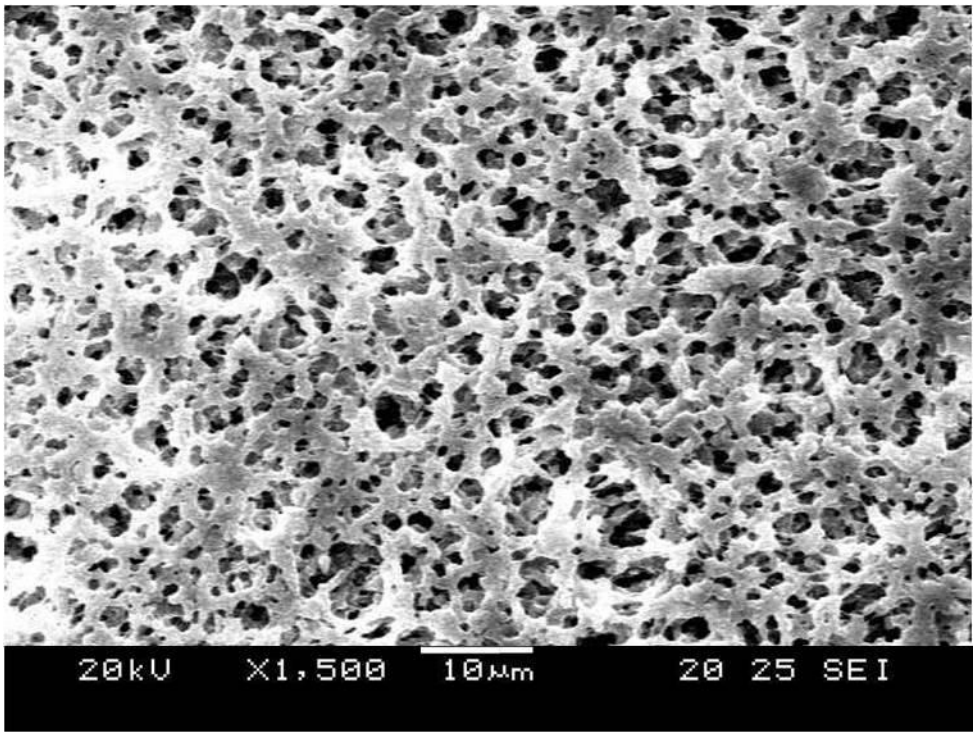

Fig. 4.3: SEM image of the PVDF membrane at 1500x.

4.4 Membrane Degradation Results

In light of the washout phenomenon in the glass fiber membranes, degradation by fouling was only performed with the PVDF membrane. The initial spreading of saltwater in the membrane was captured with time-lapse photography – see Figure 4.4. Over the course of the first hour, the saltwater (darker shading) was seen moving radially outward from the point source, as shown in frames A and B. In a membrane that had just become saturated with saltwater, the saltwater at the membrane edge could not travel further. At this point, the water evaporated leaving behind the salt. As evaporation occurred, the remaining solution approached its solubility limit. Once that threshold was reached, crystallization began. Salt crystallization became visible a little over an hour into the experiment beginning at the outer radius, as reported in frame C. As time progressed, different levels of salt buildup were observed in the membrane during the accumulation process. Referring to hour 6, frame D, the white, outermost ring was a region of pure salt crystallization with no visible water present. In this area, the membrane was rigid. The

next ring inward was a zone where the solubility limit had been reached but some visible water remained waiting to be evaporated. It was unclear if this region was still drawing replenishment water from the reservoir. The innermost section was saturated with saltwater below the solubility limit. From scanning electron microscope (SEM) images obtained with a Jeol JSM-561 SEM, the presence of salt was seen clogging the pores compared to a new membrane, Figure 4.5.

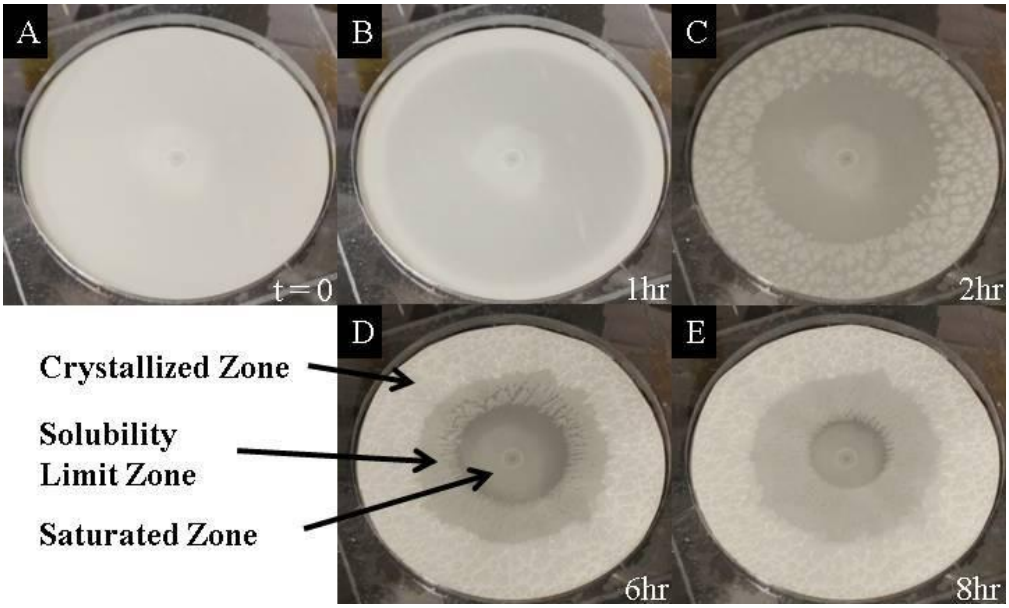

Fig. 4.4: Time-lapse imaging of salt accumulation in a PVDF membrane.

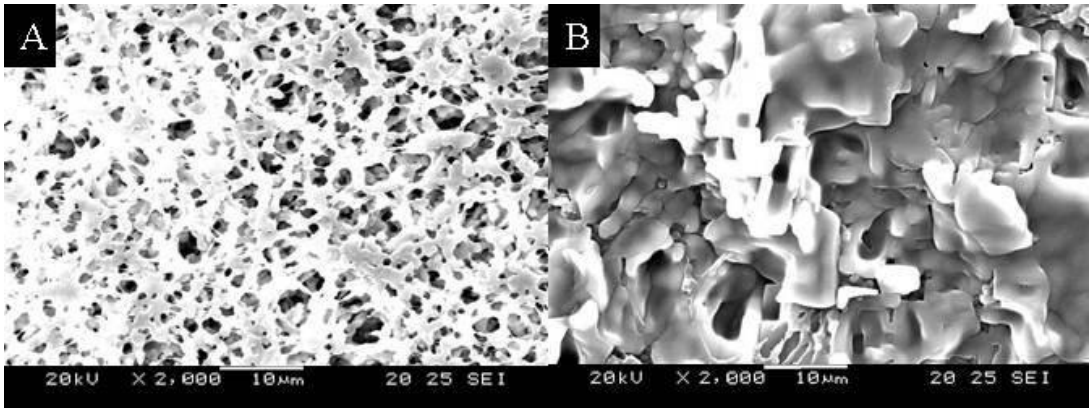

Fig. 4.5: SEM image comparison of a PVDF (a) new membrane and (b) a membrane post degradation testing.

As salt continued to be left behind as the water evaporated, the effective evaporation area decreased, thus decreasing the evaporation rate, Figure 4.6. This coincided with the inward moving salt ring from the time-lapse photography, Figure 4.4. Initially, the steady state evaporation rate from the membrane at room conditions was approximately 10 mg/min. A decreasing trend was observed until the membrane was clogged, at which time, the evaporation was steady near zero. Although the evaporation rate leveled off at about 0.8 mg/min, the membrane was considered clogged. Also, a spike in the evaporation rate can be observed in Figure 4.6 over the course of the first hour. This abnormality could potentially be attributed to the changing of reservoirs from the distilled water to the saltwater.

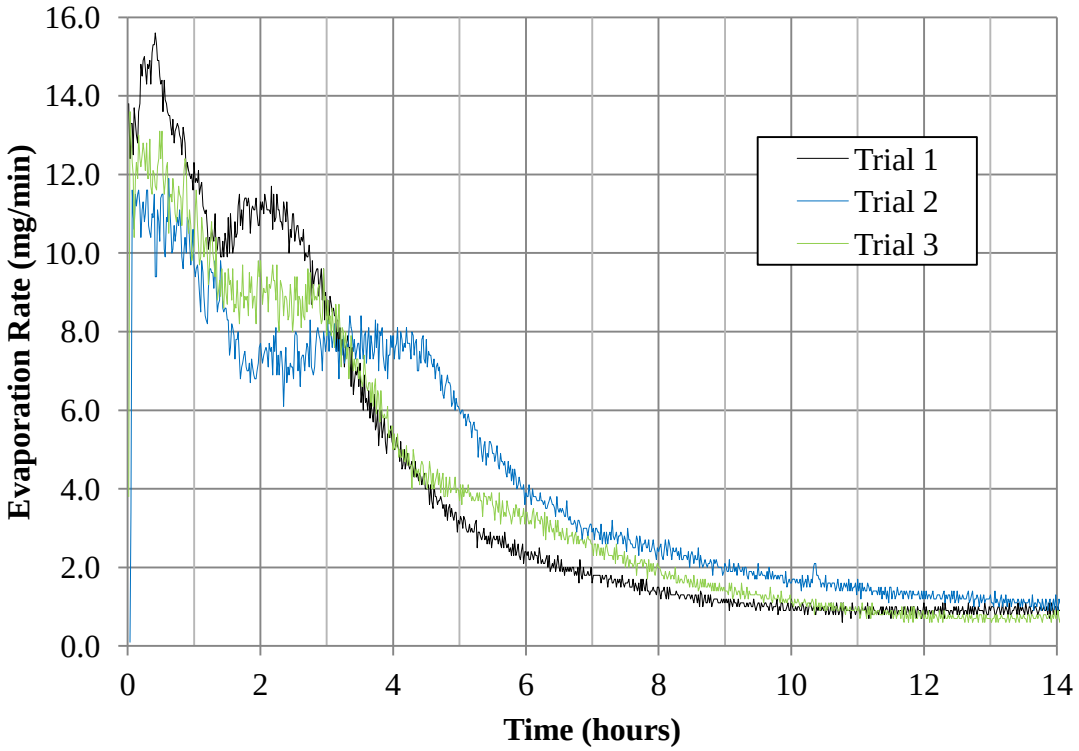

Fig. 4.6: Decrease in evaporation rate over time as salt built up in a PVDF membrane.

As expected, the evaporation rate in conjunction with the concentration of foreign particles would determine the buildup rate of material in the membrane, consequently affecting the pumping ability of the membrane. Additionally, these trials used salt, which was dissociated in the distilled water. Particles smaller than the pore size would pass easily through the membrane and collect around the outer radius much like the salt. If the solid particles were larger than the size of the pores, clogging would start at the locations of the blocked pores rather than around the outer ring. Nevertheless, as demonstrated, the integrity of the membrane is vital to maintaining the highest possible evaporation rates. Therefore, in a situation where rainwater or greywater was repurposed, it might be appropriate to first filter the water.

Chapter 5. Evaporative Cooling of an Externally Heated Surface

Previous works have used thin films of fluid on roofs to create a barrier between incoming radiation from the sun and the roof surface [53-55]. The incident energy goes first towards evaporating the fluid before it can heat the structure. While this concept has high promise to lessen air conditioning loads, a sloped roof is required so that the water may run down but if not evaporated by the roof edge, the water is wasted. When it comes to large warehouses and commercial buildings, generally, the roofs are not sloped, but rather flat, making this thin film method non-implementable. Additionally, current technology requires the use of pumps to move the water to the surface of the roof. In comparison, the proposed system would be able to passively bring the water to the roof without a pump while not wasting any.

This study addressed the capability of a roof based, passive, evaporative pumping system to alleviate thermal loadings imposed on the structure by solar radiation. The tests aimed to determine the ability of such a system to lessen roof temperatures and heat fluxes into the building compared to traditional (e.g., dark ethylene propylene diene monomer (EPDM)) and nontraditional roofs (e.g., white). To do so, an instrumented experimental setup was constructed wherein a porous membrane rested on top of an air cooled copper plate while heated by a halogen lamp from above. The evaporation rates from the membrane, plate temperature, as well as the required amount of cooling, when applicable, were measured.

5.1 Experimental Setup

The evaporation pumping system, Figure 5.1, was constructed of a porous membrane connected to a water reservoir via Tygon tubing ($1/8^{th}$ inch ID). The water reservoir rested on a balance (Denver Instruments PI - 214, range 0 to 210 g, resolution 0.1 mg), which recorded mass loss automatically to a computer file. The reservoir was covered to prevent unwanted evaporation losses leaving only a pinhole in the lid to maintain atmospheric pressure. Because all mass loss from the reservoir was due to evaporation from the membrane, the balance was considered to be recording evaporation.

Distilled water was used and, initially, the free surface of the water in the main reservoir was no higher than the membrane.

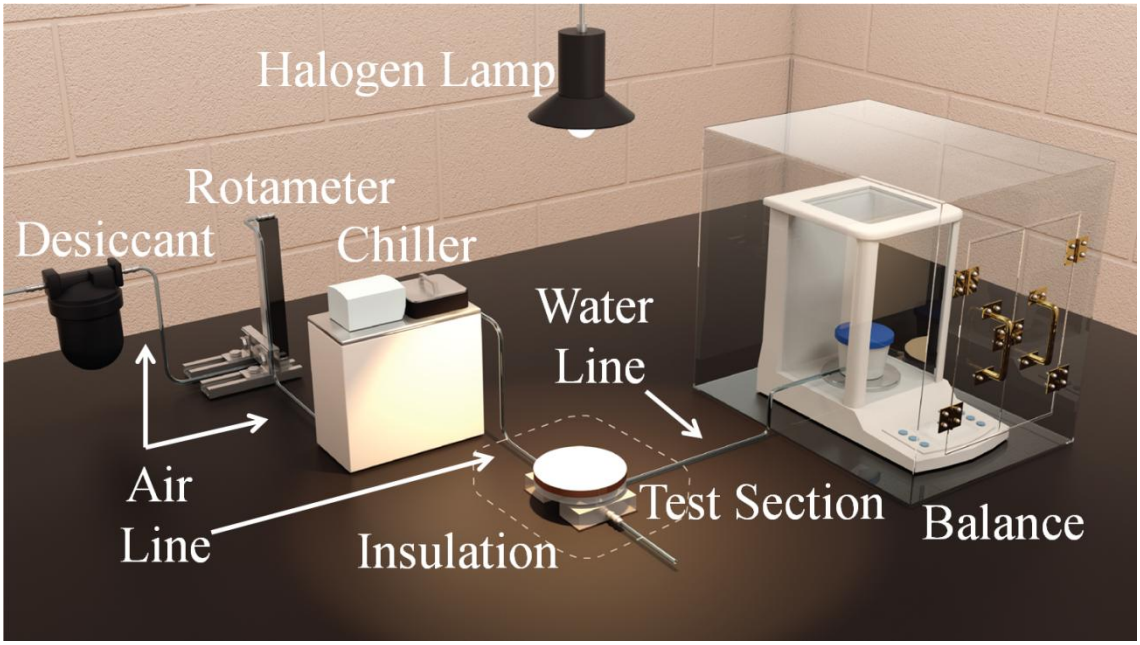

Fig. 5.1: The evaporation system setup showing the major components.

The membrane sat on a 9.1 cm diameter, 1.27 cm thick copper disk plate – a cut view of the test section, which includes all its main components, is shown in Figure 5.2. Bolted to the bottom of the copper disk was an acrylic disk with a milled evacuated space. The evacuated space measured 0.635 cm deep and was in direct contact with 64% of the bottom surface area of the copper disk. This allowed for air to flow underneath the copper to provide cooling. The air cooling was provided through a regular compressed air line, which ran through a desiccant, rotameter (Omega FL-1448-S), and chilling bath for temperature control, before reaching the test section. The flow meter allowed up to 43000 cm^3/min with a resolution of 287 cm^3/min. Through the radial center of the copper and acrylic disks, and flush with the top surface, a water line ran to the reservoir. Because this experiment was not concerned with the initial wetting phenomenon, initial wetting was provided by a second reservoir placed high above the membrane. This reservoir was tied into the main water line.

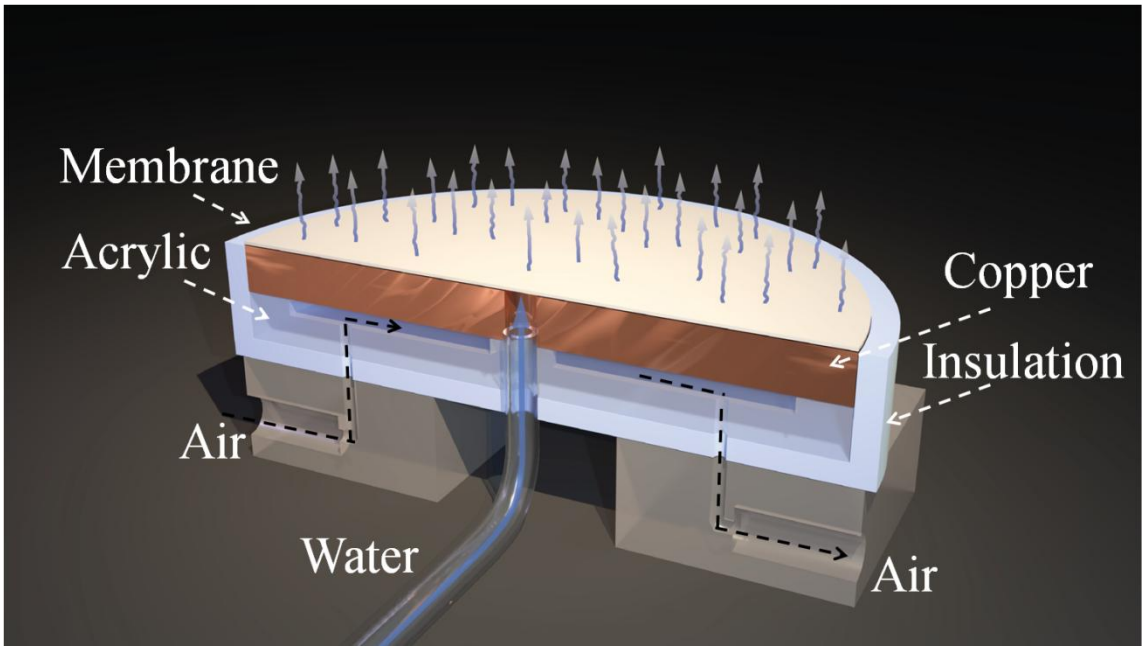

Fig. 5.2: A cross section of the test section showing the membrane sitting on top of the copper plate and acrylic disk with evacuated space. The water flow to and evaporation from the membrane can be seen along with the air path.

The evaporative surface, which was placed on top of the copper disk, was a polyvinylidene fluoride (PVDF) Millipore Durapore membrane filter with a porosity of 0.7, diameter of 9 cm, and thickness of 135 μm. The pore structure was of a random nature with a manufacturer specified pore size of 0.65 μm - scanning electron microscope (SEM) images showed that the pore size reached up to 3 μm.

To simulate solar heating, a halogen lamp (Bayco SL-1082) was placed 0.43 m above the membrane. The lamp had three settings allowing for 250, 500, and 750 W. Because the actual heat flux reaching the test section was initially unknown, an Eppley precision spectral pyranometer was used to create a 2D map characterizing the flux intensity that would be imposed on the membrane at the selected vertical distance (i.e., 0.43 m). Based on the lamp's power and the 2D map, made every square inch, the exact locations within a horizontal plane below the lamp were determined that would provide

uniform fluxes on the test section – the heat fluxes imposed onto the test section were 130, 315, 434 ± 5% W/m^2. A complete analysis regarding the lamp intensity's calibration can be found in Appendix D. The disk's side and bottom were well insulated to ensure all heat flow that entered the copper disk went to the airstream.

As shown later, the present study also compared the thermal shielding performance of the evaporative (i.e., wet) membrane with the dry membrane, which was used to simulate a white roof. Therefore, since the surface properties of the wet vs. dry membrane were different, it was necessary to evaluate properties such as reflectivity and absorptivity for both surfaces. The reflectivity of the membrane on copper, wet and dry, was measured with a spectrophotometer (Optronics Laboratories, OL-750) and are shown in Figure 5.3. To the visible eye, when the membrane was dry, it was white opaque whereas when wet, the membrane was transparent. For the wet membrane, the water absorption bands can clearly be seen as a trough between 1400 and 1500 nm as well as between 1900 and 2000nm. The location of these troughs coincide where the water absorption bands exists for solar radiation. When exposed to a halogen lamp with a spectrum between wavelengths of 350 and 2500 nm, the reflectance of the wet and dry membranes was found to be 0.7 and 0.92, respectively. This measurement was used to calculate the absorptivity of the wet and dry membranes to be 0.3 and 0.08, respectively. Furthermore, it should be noted that the solar irradiance spectrum of the sun is mimicked by a halogen light making a halogen lamp an appropriate choice of lightening for this experiment. A complete analysis regarding the calculation of reflectivity and absorptivity can be found in Appendix D.

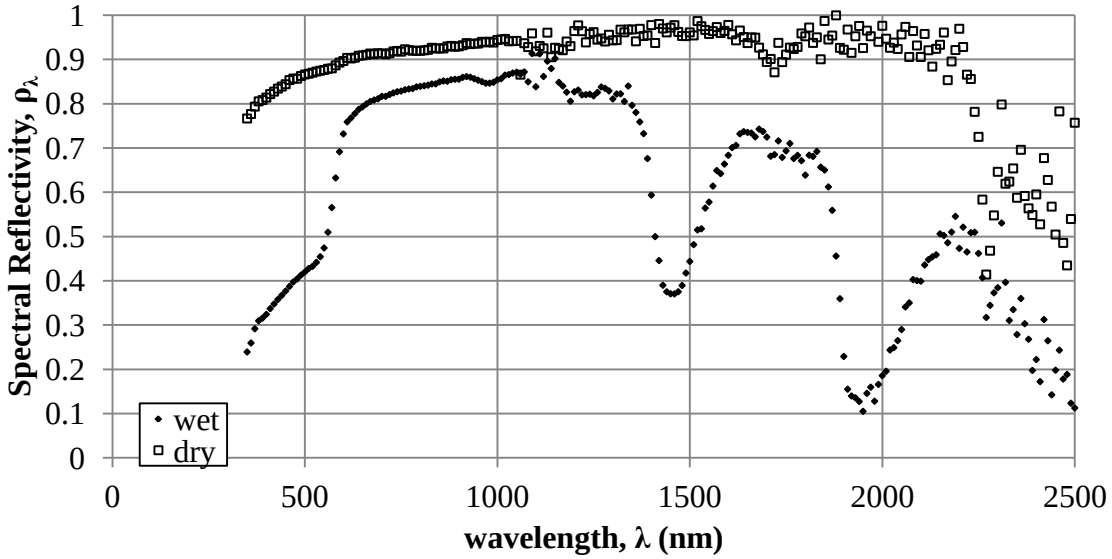

Fig. 5.3: Spectral reflectance for both a wet and dry membrane when backed by copper.

Using thermocouples, which had a calibrated uncertainty of 0.12 °C at 95% confidence, the temperature of the copper disk was measured at its midplane thickness at a radius of 2.5 cm in three locations, above the air inlet, halfway along the air flow path, and at the air outlet. A thermocouple was also placed right above the membrane's surface to measure the air temperature. Additionally, thermocouples measured the air temperature at the inlet and outlet of the acrylic disk. From the measurement of the air temperatures, the cooling load provided to the copper by the air could be assessed using an energy balance, $q = \dot{m} \times c_p \times (T_{out} - T_{in})$, where q was the cooling load that would be needed to maintain the particular copper disk temperature, $\dot{m}$ was the mass flow rate of the air, c_p was the specific heat of air, and T was the inlet and out temperatures of the air.

5.2 Experimental Results

The first series of tests performed aimed to study the effect of the lamp power output on the evaporation rate of the membrane, which was not subjected to air-cooling underneath. In this case, the bottom surface of the copper disk was insulated. This experiment was meant to mimic a real situation of the sun shining on a roof. Also, it created a baseline for evaporation rate and plate temperature when exposed to various

lamp intensities for comparison to future experimental boundary conditions. The evaporation data displaying the steady state behavior over time can be seen in Figure 5.4 while the results indicated that increasing the power supplied by the lamp onto the test section increased the evaporation rate. With this relationship being somewhat expected, perhaps more interesting was the fact that, in conjunction with the increase in evaporation rate, the increase in lamp intensity also caused an increase in the temperature of the copper plate, as shown in Figure 5.5.

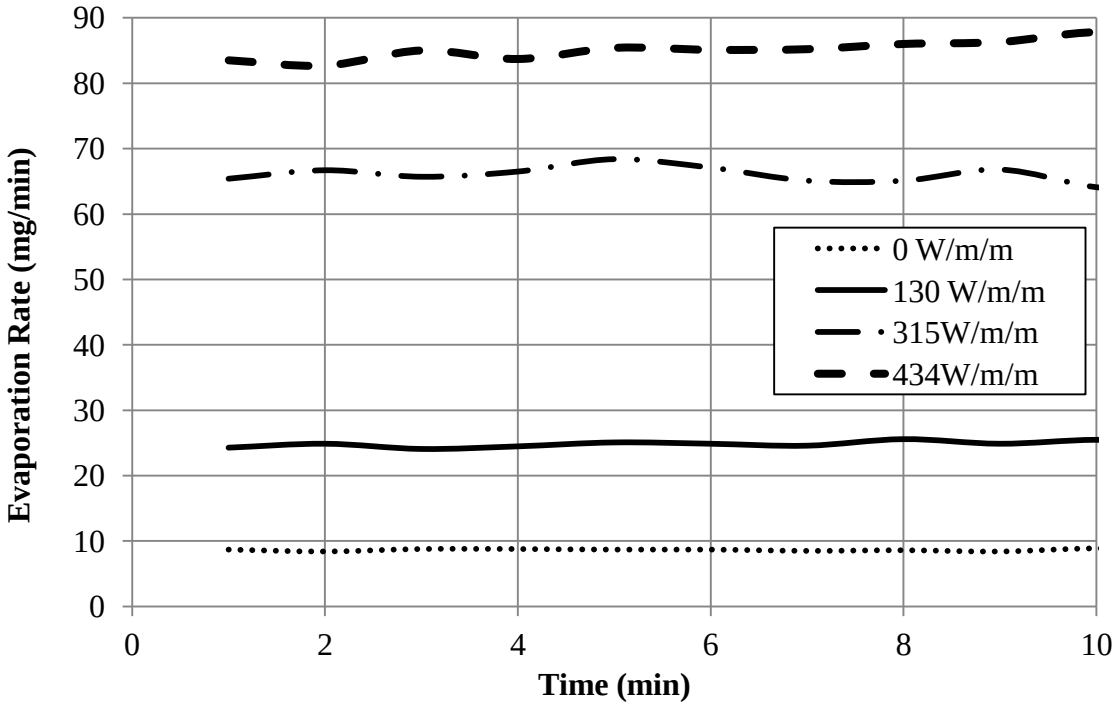

Fig. 5.4: Evaporation rate with respect to time for different lamp power outputs showing steady state.

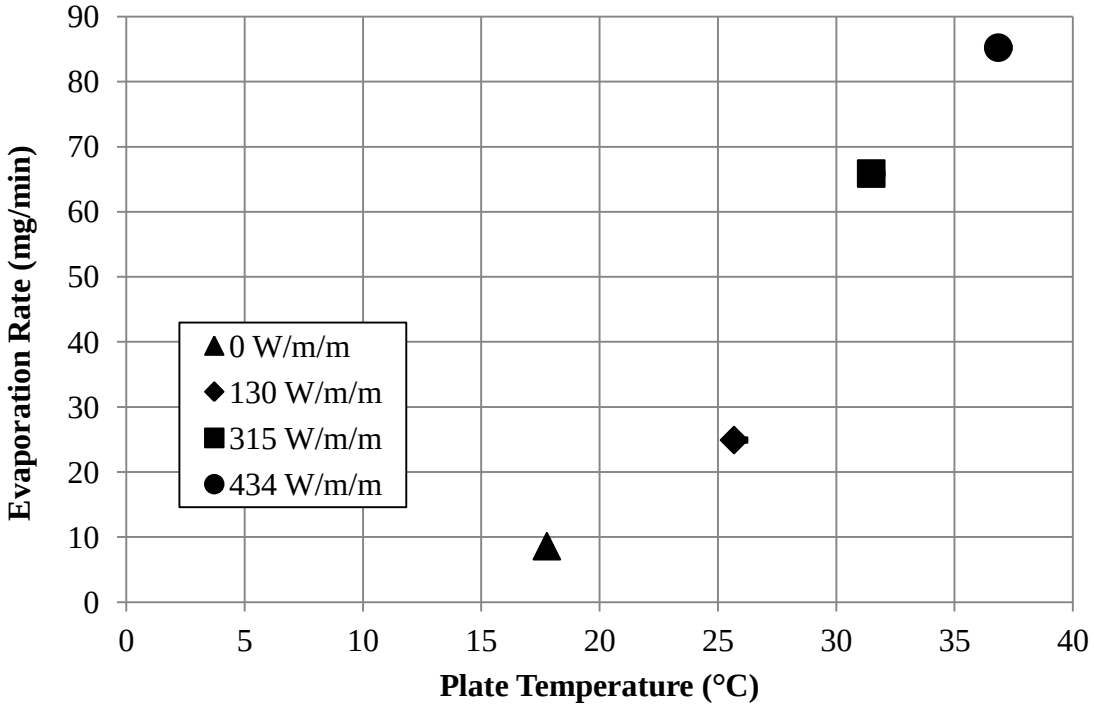

Fig. 5.5: Temperature of the copper plate test section under various loading conditions imposed by the lamp for an evaporating membrane at steady state operations.

Next, the performance of the evaporation system on plate temperature was compared against other possible roof configurations, such as white and dark roofs, with no cooling provided underneath. The measured experimental results for the evaporating membrane, seen in Figure 5.6 as solid circular markers, showed an increase in plate temperature as a function of lamp intensity. To mimic a white roof, a dry membrane replaced the evaporating membrane for the testing of different lamp intensities – these measurements are represented by the solid squares on Figure 5.6. Recall that the dry membrane was white as compared to a wet membrane, which was transparent, except for the copper disk underneath, which ultimately, enforced a zero transmissivity for the wet membrane/copper disk assembly. The experimental results for the plate temperature for the dry membrane also showed an increase with lamp intensity. To capture the behavior of a system with a dark surface, the performance of ethylene propylene diene monomer (EPDM), a common roofing material, was estimated using its known properties [roof 2].

In this case, its surface temperature was simulated using an energy balance for the various lamp intensities, as seen in Figure 5.6 as open triangular markers. Therefore, these were not measured values, but rather estimated points. The results indicated that the temperature of the copper plate was considerably lower when employing the evaporating membrane as compared to the tested dry membrane (i.e., white roof) and the simulated EPDM (i.e., dark roof) over the range of intensities considered in the tests. Moreover, as the lamp intensity increased, the temperature disparity between the roofs widened. At a maximum tested intensity of 434 W/m^2, the simulated EPDM was 24°C above the evaporation system. Therefore, if the copper test section was to be considered a roof with the lamp being the sun, a roof employing the evaporation system would keep the roof temperature noticeably lower. This is important when considering the conduction of energy through the roofing structure that the air conditioning must then cool.

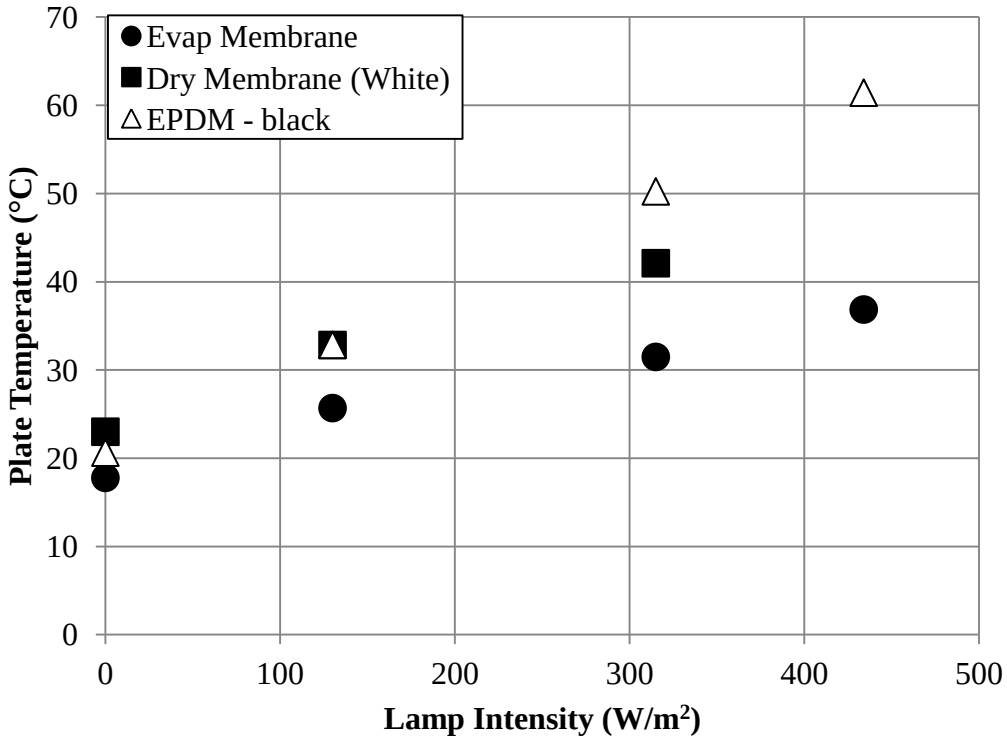

Fig. 5.6: Plate temperature for an evaporating and dry membrane along with the calculated EPDM covered copper plate temperature under different lamp intensities.

The results above suggested that the lamp intensity dictated the plate temperature and the evaporation rate when no cooling was provided underneath by flowing air. While this observation was interesting in itself, it did not indicate which of these two factors was more influential on the evaporation rate. However, if air cooling was applied to the bottom surface of the copper plate, and its cooling capacity was adjusted by varying the air flow rate and inlet temperature, the copper plate temperature became independent of the lamp wattage. To further explore this, a new set of tests was performed for a given dissipation of the halogen lamp (i.e., 315 W/m^2) and several temperature values for the copper plate. The results, which are represented by the solid circles on Figure 5.7, show that the evaporation rate can be highly affected by the plate temperature - for a lamp power of 315 W/m^2, as the plate temperature was decreased, the evaporation rate followed suit. This suggested a greater dependence of the evaporation rate on the temperature of the plate rather than the imposed lamp intensity.

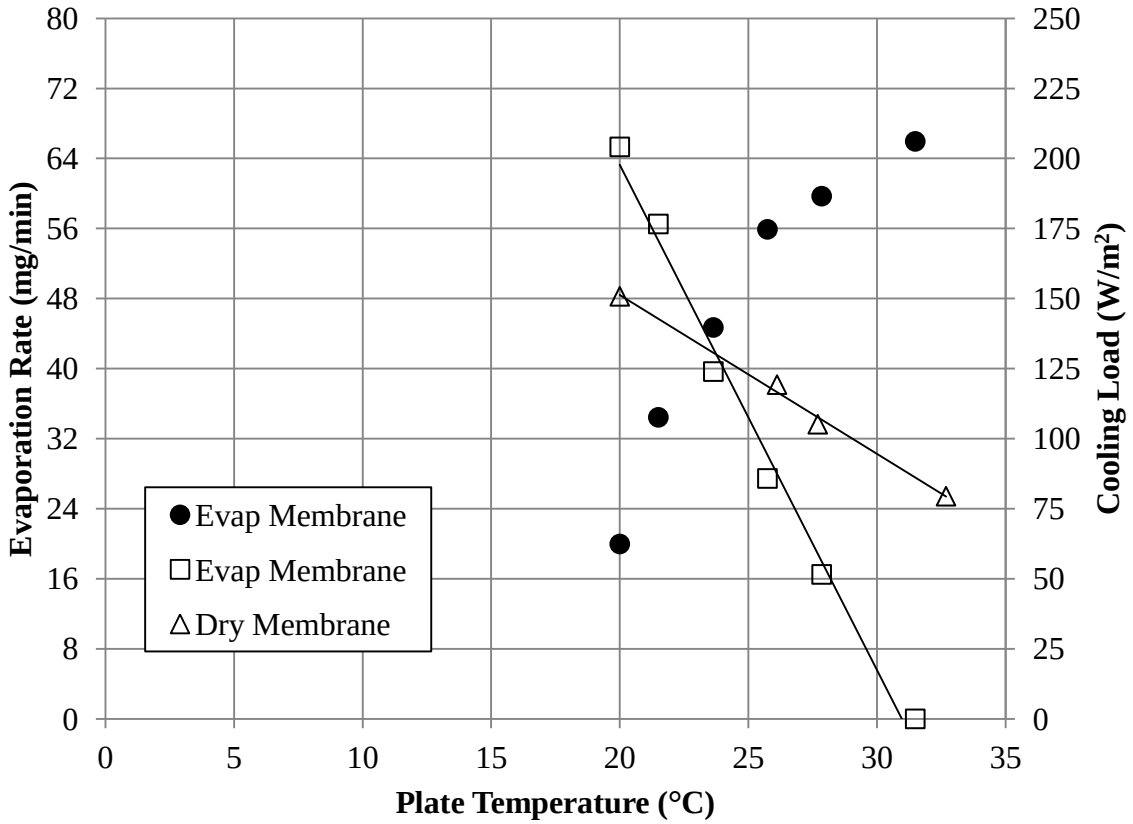

Fig. 5.7: Effect of plate temperature on evaporation rate (right vertical axis, solid markers) and cooling required to maintain particular plate temperatures for evaporating and dry membranes (left vertical axis, open markers), all for a lamp intensity of 315 W/m^2.

Also interesting was the required amount of cooling needed to lower the plate temperature and the air temperature increase as it flowed under the plate - these are also depicted in Figure 5.7 through the open markers for the wet and dry membranes in the right axis. The cooling required was calculated by applying an energy balance, $q = \dot{m} \times c_p \times (T_{out}–T_{in})$ to the air flowing underneath the test section. Undoubtedly, the most interesting aspect of this data was that the curves representing the wet and dry membranes crossed each other for a plate temperature around ~ 24°C. This indicated that, at higher plate temperatures (e.g., > 24°C) the evaporative membrane was able to

maintain a particular plate temperature with less cooling aid than the dry membrane. As the plate temperature was required to reach lower values (i.e., < 24°C), the dry membrane required comparatively less cooling load than the evaporative membrane to maintain lower plate temperatures.

This behavior can be potentially explained by analyzing the direct relationship between the plate temperature and the evaporation rate. As the evaporation rate was restricted (i.e., low plate temperatures), it was unable to carry away as much energy from the plate thus requiring greater cooling loads. Therefore, it was shown that for these conditions, the dry membrane started to outperform (i.e., require less cooling load) the evaporating membrane once the plate temperature dropped below 24°C. Arguably, the intersection of the performance of the two systems would shift relative to plate temperature based on the imposed thermal load of the lamp. Extrapolating the thought further, if the evaporation rate was hindered for a reason other than artificially lowering the plate temperature, perhaps by fouling of the membrane, neglecting changes in the optical properties, the temperature of the plate possibly would increase.

To show an extreme case of the outperformance of the dry membrane over the evaporating membrane, the plate temperature was kept at 20°C for the data shown in Figure 5.8, and the cooling load was measured for different lamp intensities. Again, cooling was accomplished by flowing chilled air through the acrylic chamber underneath the copper plate. The gap in cooling requirements between the dry and evaporating membranes increased with increasing lamp intensity. At a maximum tested intensity of 434 W/m^2, an additional 125 W/m^2 was required to maintain the plate temperature for the evaporating membrane. It should be noted that since the plate was pinned to 20°C, the evaporation rate was severely impacted. At this plate temperature, for all tests, the evaporation rate was measured to be roughly 15 mg/min, regardless of the lamp intensity, which is relatively low when compared with the rates reported in Figure 5.6.

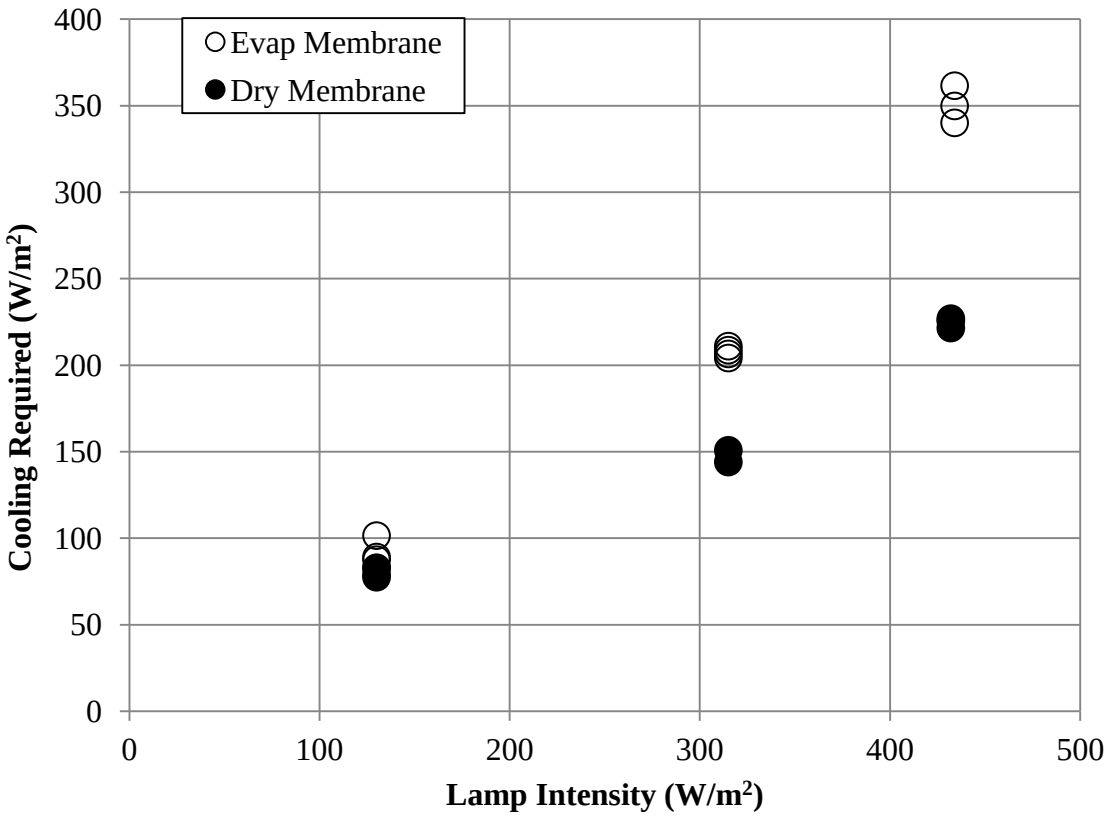

Fig. 5.8: Cooling required to maintain a constant plate temperature of 20°C for an evaporating and dry membrane.

Chapter 6. Resource Allocation Analyses

The evaporation system discussed in this dissertation used a number of resources, i.e., water, roof space and solar energy, which could potentially be purposed in other ways. It is the goal of this section to explore the justification of those named resources to the evaporative system.

6.1 Water Consumption

To begin with, the water consumption was simulated under the imposed solar radiation of a typical, clear, summer day in Austin, TX [57], where direct radiation fluxes reach roughly 900 W/m^2. From the previous experiment, §5, the measured evaporation rate for various lamp intensities when the test section was not air cooled (i.e., referring back to Figure 5.5) were linearly extrapolated to estimate the evaporation rates for all imposed solar radiation. For such fluxes, it was estimated that the system would evaporate water at a peak rate of 0.0122 $kg/min/m^2$. Integrating the resultant normalized evaporation rate over the course of a day, the total water consumption of the system by evaporation would be 7.4 $kg/m^2/day$ (1.96 $gallons/m^2/day$), as shown in Figure 6.1.

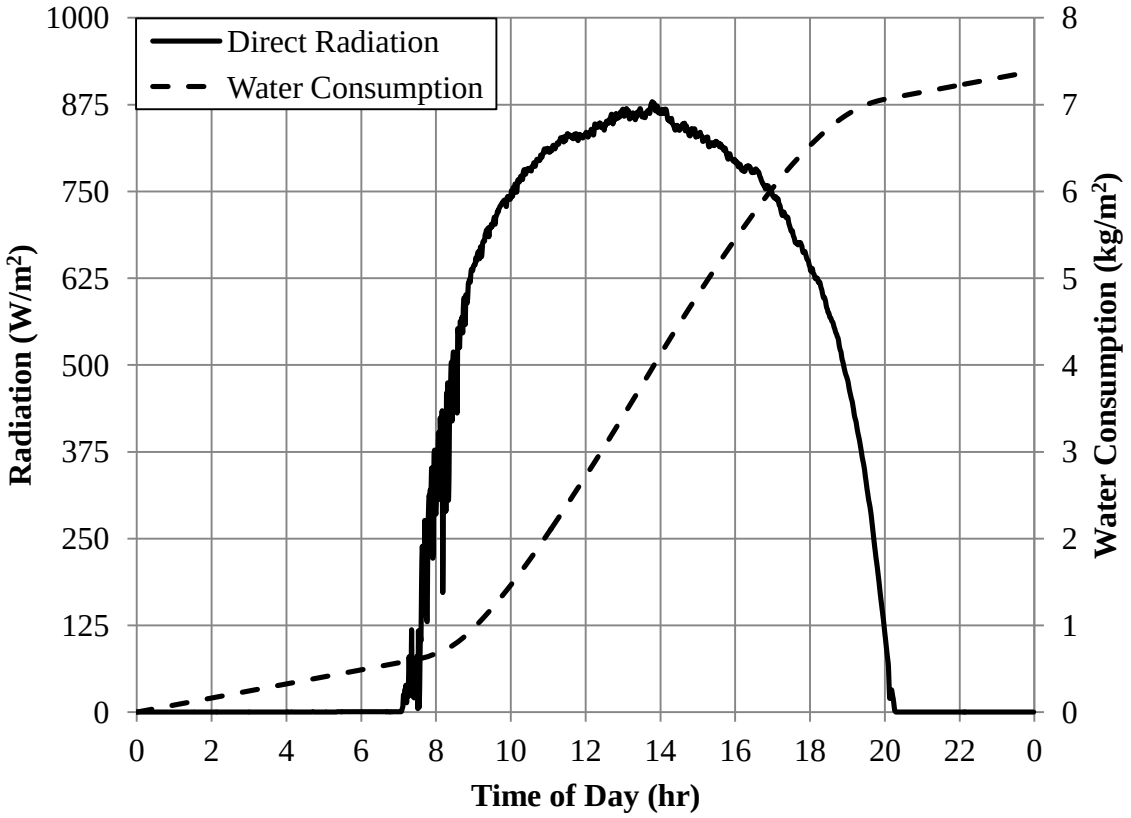

Fig. 6.1: Total water consumption over the course of a typical August day in Austin, TX (Aug 2, 2012).

While the evaporative system uses water for cooling, to offset electricity usage, that water could have been used in electricity production. Torcellini, et al. [58] reported that the national average to produce 1 kWh of electricity requires 2 gallons of water. This water usage occurs for different reasons related specifically to the type of generation, but ultimately it is evaporated. While the actual amount of water used per kWh varies widely based on generation type and location, the 2 gallons/kWh average comes from the U.S. aggregated average of total water consumption which is 0.47 and 18.0 gallons/kWh for thermoelectric and hydroelectric plants, respectively. With 89% of generation coming from thermoelectric systems, evaporative losses occur during the condenser phase of the cycle. Traditionally, plants pulled cooling water from nearby bodies of water then dumped it back in, elevating the body temperature which caused increase evaporation

rates. Because of the elevated water temperatures, it became apparent that putting the water directly back into the source body was detrimental impacts on the ecosystem; the cooling tower is now favored. In the towers, though, the water is evaporated at high rates to dissipate heat. Hydroelectric power production, on the other hand, which makes up 9% of generation, directly uses water for generation but does not consume it. Its water losses occur in the upstream reservoirs. Generally, manmade lakes are created to supply the hydroelectric power stations with water but due to their large footprint, the evaporation is much greater than had the landscape been left undisturbed. It should be noted that water related to fuel mining operations were not included in the 2 gallons/kWh average.

With a basis of the evaporation system's water consumption (i.e., 1.96 gallons/m^2/day) and the national average for electricity production (i.e., 2 gallons/kWh), a direct comparison can be made for water usage. For simplicity, the evaporation system's usage, over the course of a day, is rounded to 2 gallons of water for every square meter it is implemented on a roof. Those 2 gallons could alternatively be used to produce 1 kWh of electricity. Considering an air conditioning system with a coefficient of performance (COP) equal to 3, to justify the evaporation system's usage, it would have to offset 3 kWh worth of cooling per square meter of implementation over the course of a day. Referring to Figure 5.7, with no cooling provided to the evaporation system with 315 W/m^2 imposed by the lamp, the dry membrane, representing a white roof, required roughly 88 W/m^2 (2.1 kWh/m^2/day) of cooling to maintain an equal plate temperature. While this is lower than the required 3 kWh for justification, the lamp intensity was about one third of peak solar radiation conditions. At the given lamp intensity, with an roof albedo a little higher where the cooling requirement would 125 W/m^2 , the evaporation system would be able to compete with an air conditioning system with a COP of 3 in terms of water consumption. When considering the evaporation system in use verse a dark roof, which has a much higher absorption than a white roof, it is believed that the water usage would easily meet the justification criteria. It should be noted that when using a copper plate, minimal insulation resistance was provided by the plate. If a commercial roof with insulation up to code (i.e., R10 [59]) was considered the evaporation comparative

effectiveness would be reduced. With this in mind, implementation might best be suited for low insulated roofs.

6.2 Solar Radiation Usage

Another allocation of resources concerning roof space and solar radiation would be the installation of photovoltaic (PV) systems for electricity generation. At standard operating conditions, commercial c-Si PV systems have an efficiency of ~11% [60]. If a c-Si PV system was installed on a typical, clear Austin summer day, the electricity production can be approximated as seen in Figure 6.2. The electricity production peaks at roughly 0.095 kW/m^2 corresponding with the highest direct radiation, occurring around 2 pm. A direct comparison is difficult because experimental data was not measured for the cooling loads for the albedo associated with a PV array unlike the white roof which was mimicked by the dry membrane, referring to Figure 5.7. Dominguez, et al. [61] reported that flat PV and dark roofs had no noticeable difference in roof surface temperatures thus the heat transfer into the structure would be comparable for PV covered roofs and dark albedos. However, an attempt is made to compare the evaporation system with a fictionally PV system requiring the same cooling load as the dry membrane (white roof) when the roof temperature was at the measured natural temperature associated with evaporation at 315 W/m^2 imposed, Referring to Figure 5.5. At 315 W/m^2, the PV system would be generating ~35 W/m^2. Using the dry membrane cooling load of 88 W/m^2, an air conditioning system with a COP of ~2.5 would be needed to consider the performances of the two systems equal. With a higher efficiency air conditioner (COP > 2.5), the PV would be a better choice. However, because the expected absorption of a real PV system is anticipated to be much higher than the white roof scenario presented, the evaporation system is predictable to outperform the PV electricity generation even when powering air conditioning units with higher COP. Furthermore, it is envisioned that the evaporation system would be able to cover more roof surface area than PV systems.

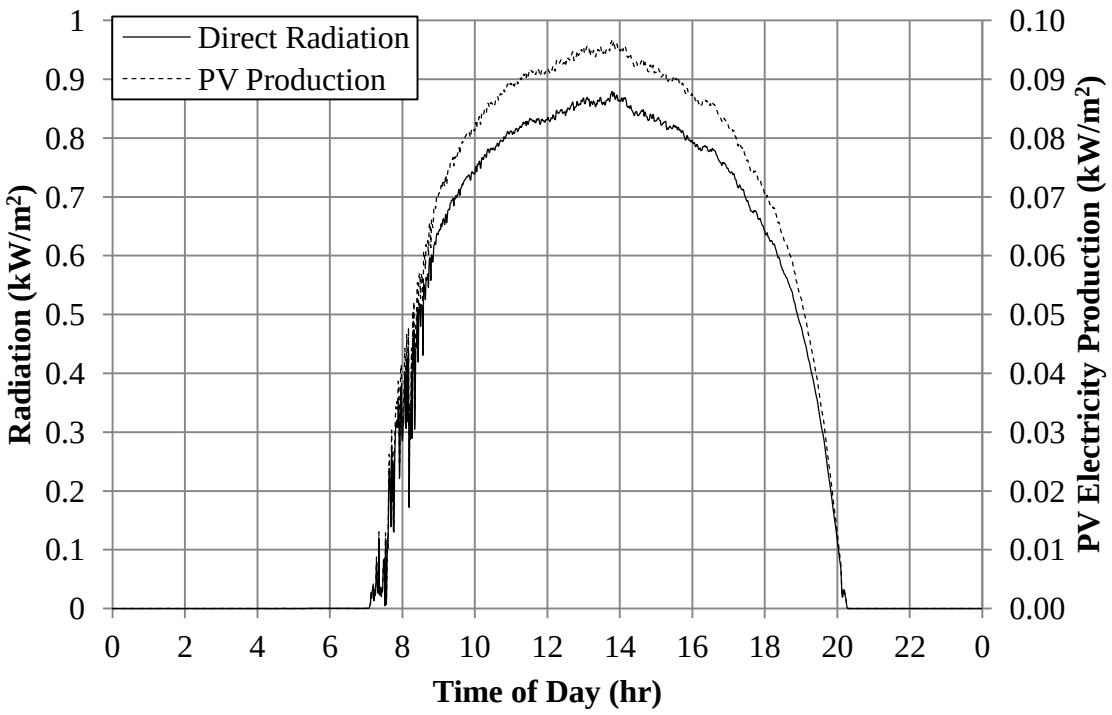

Fig. 6.2: Electricity general for a c-Si PV panel at 11% efficiency.

6.3 Cost Analysis

In this section, an analysis will be performed to compare the cost of the membrane verse a PV on a square meter basis. The price of the PV system will reflect its price per W when installed. However, the costs associated with the evaporation system will only reflect the price of the membrane.

The Millipore PVDF membranes used in this study were circular with a diameter of 9 cm coming at a cost of $\$560/m^2$. For applications, such as what was described in this dissertation, multiple point sources most likely would be arranged in an array based off of minimum desired local evaporation rate. For that, it might be more appropriate to use a membrane sheet rather than discs. Fortunately, Millipore offers the same membrane in sheets measuring 0.304 by 3 m costing roughly $\$306/m^2$.

The price of installed PV continues to decline year after year with the most recent data showing an 11-14% decrease from 2010 to 2011 [62]. Among the systems installed

in 2011, residential and commercial units less than 10 kW were averaging $6.13/W while larger commercial units up to 100 kW were $4.87/W. Using the standard test conditions (STC), which correspond to 1000 W/m^2 irradiance, efficiencies of c-Si PV systems can reach 14% [60]. This would mean 10 kW systems would require ~71.4 m^2 while larger, 100 kW systems would need an area of ~714 m^2. Based on the installed pricing, 10 kW and 100 kW systems would cost roughly $858/$m^2$ and $681/$m^2$, respectively.

The cost of the membrane was 55-64% the cost of installed solar. While the membrane did not include the cost of other components or installation, there is plenty of capital room to work with. It should also be considered that it is not known how often this membrane would need to be replaced when exposed to true environmental conditions as this was not its intended purpose. Additionally, with the declining price trend of PV technology, the price gap will close soon. To compete with both the declining price of PV as well as with membrane integrity concerns, other porous media options should be explored. Recalling the various porous rocks Wanphen and Nagano [50] used, it might be appropriate to explore those options for their cost effectiveness and ability to withstand environmental exposure.

Chapter 7. Comments on Evaporation

7.1 Evaporation

Evaporation from undisturbed pools of water into still air has been investigated thoroughly for its applications ranging from swimming pools to spent nuclear fuel pools [Shah]. While many empirical correlations have been presented for evaporation, they are very specific for their conditions of temperatures, pressures and humidity. In Table 1, several empirical correlations are presented for undisturbed pool water evaporation. Resultant evaporation rates are reported for environmental conditioned measured during laboratory experiments for a room temperature of 24 °C, humidity of 50%, room pressure of 101 kPa and room wind speed of 0.2 m/s. The results, excluding Rohwer et al [63] are comparable to those obtained in the evaporation experiments. In Chapter 2, using a glass fiber, 5.08 cm diameter membrane, normalized evaporation rates were measured to be 0.18 mg/min/cm^2. This was the smallest membrane size tested but an increasing trend was shown for decreasing membrane size, Figure 2.6. Following the trend, the maximum normalized evaporation rate, corresponding with evaporation at the center of the point source, would be ~0.216 mg/min/cm^2. For the study conducted in Chapter 5, using the PVDF membrane, with no heat flux or cooling imposed, the normalized evaporation rate was 0.157 mg/min/cm^2, however, this was for a plate temperature of ~18 °C. Because the evaporation rate was tied to the substrate temperature, as demonstrated in Chapter 5, a more direction comparison is done when the evaporation rate is estimated for the substrate temperature of Chapter 2. With this in mind, with the substrate temperature of 23 °C, the normalized evaporation rate was figured to be 0.236 mg/min/cm^2. Both experimental normalized evaporation rates fall within the empirical correlations. Additionally, the normalized evaporation rates fell within the range calculated using Fick's Law of Diffusion [64].

Table 7.1: Normalized evaporation rates for correlations of evaporation for still pools.

Correlation	Equation	Normalized Evaporation Rate ($mg/min/cm^2$)
Smith et al. [65]	$E_{.smith} := \frac{.76 \cdot \left(.089 \frac{m}{s} + .0782 \cdot u \right) \left(p_{.sat} - p_{.par} \right)}{h_{fg}}$	0.175
Biasin and Krumme [66]	$E_{.biasin} := \left[-0.059 + 0.000079 \cdot \left(\frac{p_{.sat}}{Pa} - \frac{p_{.par}}{Pa} \right) \right] \cdot \frac{kg}{m^2 \cdot hr}$	0.098
Rohwer [63]	$E_{.rohwer} := 0.08 \left(\frac{T_{.water}}{K} - \frac{T_{.r}}{K} + 3 \right)^{\frac{2}{3}} \cdot \left(\frac{p_{.sat} - p_{.par}}{Pa} \right) \cdot \frac{kg}{m^2 \cdot hr}$	413.6
Boelter [67]	$E_{.boelter} := 0.0000162 \cdot \left[\frac{\left(p_{.sat} - p_{.par} \right)}{Pa} \right]^{1.22} \cdot \frac{kg}{m^2 \cdot hr}$	0.201
Himus and Hinchley [68]	$E_{.himus} := 0.0000258 \cdot \left[\frac{\left(p_{.sat} - p_{.par} \right)}{Pa} \right]^{1.2} \cdot \frac{kg}{m^2 \cdot hr}$	0.277
Leven [69]	$E_{.leven} := 0.00000945 \cdot \left[\frac{\left(p_{.sat} - p_{.par} \right)}{Pa} \right]^{1.3} \cdot \frac{kg}{m^2 \cdot hr}$	0.21
Box [70]	$E_{.box} := 0.0000778 \cdot \frac{p_{.sat} - p_{.par}}{Pa} \cdot \frac{kg}{m^2 \cdot hr}$	0.193
Fick's Law Diffusion [64]	$E := \frac{C \cdot D_{.AB}}{t} \cdot \ln \left(\frac{1 - x_{.surf}}{1 - x_{.water}} \right) \cdot M_{.water}$	0.1 – 0.39

where E is the normalized evaporation rate, u is the wind speed, p_{sat} is the saturation pressure, p_{par} is the partial pressure at room temperature and humidity, h_{fg} is the change in enthalpy of water from a liquid to a gas, T_{water} is the temperature of the pool and T_r is the

room temperature. For Fick's Law of Diffusion, C is a concentration per volume, D_{AB} is a diffusion coefficient, x is a pressure ratio and t is the boundary layer thickness.

7.2 Atmospheric Conditions

Evaporation is based on the ability of the medium to receive that which is being evaporated. This ability is based on conditions such as pressure, temperature and humidity in the environment. As seen in the previous section, all of the correlations were based on a difference between the saturation and partial pressures. The saturation pressure is directly related to the temperature so an increase in temperature would increase the saturation pressure. The partial pressure is also related to the humidity in the air. If, for example, the air was already saturated with water, referring to a humidity of 100%, the air would not be able to evaporate additional water vapor.

While only one of the correlations incorporated wind velocity, most of the correlations were meant for still conditions. From a physical perspective, when the air is over a water surface, evaporation is saturating the air. With a wind velocity, the space over the water is being refreshed with air of lower partial pressure thus allowing for higher evaporation rates. To better understand the influence of wind velocity, the boundary layer thickness of Fick's Law of Diffusion is used. The boundary layer is a function of Reynolds Number which is a function of velocity thus boundary layer thickness is ultimately a function of velocity. With increased velocity, the boundary layer thickness decreases which causes an increase in the evaporation rate.

Chapter 8. Conclusion

The biomimicing of transpiration based systems for fluid transport has been investigated by several groups for applications ranging from energy harvesting [39] to DNA and cell adhesion studies [43].The methods to produce prototype devices, however, have usually required microfabrication techniques which can be costly and time consuming. Additionally, because of their designed applications, fluid transport has only been on a small scale. While most of the work uses the evaporation phenomenon part of transpiration, little attention has been paid to the energy removal capability of phase change. One sector that could greatly benefit from the energy dissipation of evaporation is the commercial building sector which has high cooling requirements [19]. Many groups have investigated, both numerically and experimentally, the integration of evaporation into roof cooling [46-51]. While most have experienced some degree of success with the lowering of roof surface temperatures which translates to lower heat flux into the structure, components such as pumps and control systems are required for moving the water to and dispersion it over the roof. Furthermore, slanted roofs are needed and the potential exists for the water to be wasted if not evaporated by the roof's edge. Drawing from the lessons learned related to biomimicing transpiration and with an application towards aiding building cooling, it was the purpose of this research to develop a passively pumping, evaporation based system for roof integration to create a solar barrier.

8.1 Summary of the Results Obtained

8.1.1 Characterization of Geometric Parameters

In general, the system developed consisted of a porous membrane connected to a water reservoir by means of a feeding tube which did not require microfabrication. However, to implement such a system, the effects of the component had to be understood first. A multipart investigation was performed to systematically analyze the influence of component properties on the system's performance. In the first study, the evaporation membrane (Fisherbrand Glass Fiber Filter Circles G6) was connected to a fluid reservoir

by means of PEEK micro tubing. While measuring evaporation rate from the membrane and the suction pressure, the diameter and length of the tubing was varied in efforts to constrict the flow. It was found that with increased hydrodynamic resistances, i.e. small diameters and longer lengths, the evaporation rate was unaffected for the range of parameters tested. Conversely, the suction pressure, which can be thought of as potential pumping height, was decreased by the hydro resistances. Also of interest was that surface areas did not affect suction pressures. Additionally, the membrane surface area's influence on evaporation rates was determined. With expected resulting trends, the evaporation rate decreased with decreasing surface area. When the evaporation rates were normalized, however, smaller areas had higher rates. This led to the conclusion that a critical radius would exist where the fluid would be totally evaporated when drawing from a point source. This has implications for spacing when aligned in an array where local, acceptable evaporation rates must be balanced against the desired effectiveness of fluid transport or thermal cooling.

8.1.2 Evaporative Cooling of an Internally Heated Surface

The second study retrofitted the evaporation system to be placed on a uniform heat flux source. While a membrane still drew from a fluid reservoir, the tubing's hydraulic resistance was made negligible as to study the effect of heating the system. Of concern in this investigation were the evaporation rates and suction pressures for various heater powers and membrane areas. Furthermore, the temperature of the heater was measured with and without evaporation being applied. Results of evaporation rates with increasing power were as to be expected with a direct relationship. As in the previous study, the normalized evaporation rate increased with decreasing membrane areas. When the suction pressure was measured for various powers supplied to the heater, no discernible differences were found. This leads to the conclusion that suction pressure is a property of the membrane structure rather than the extensive properties. Concerning the temperature of the heater, with the evaporation system in operation and the heat turned off, the temperature was recorded lower than room temperature. Moreover, when the

heater was powered, the evaporation system maintained a considerably lower heater temperature than had natural convection solely been relied upon for cooling.

8.1.3 Membrane Degradation Study

Because membranes were used throughout this study and when considering the applications where repurposed water might be used, it was deemed appropriate to investigate the membrane's susceptibility to degradation and fouling. Using a setup similar to the first study, the system was allowed to evaporate continuously for up to a week. At random, unpredictable times, the evaporation rate would drop to zero and remain. Using both a new membrane and post test membrane that had exhibited the collapse of evaporation rates, they were viewed under a SEM. The structure of the membrane was glass fibers which created a non-rigid porous matrix. Compared to the new membrane, the post test membrane showed a lower fiber density. When comparing different locations within a post test membrane, it was seen that at locations closer to where the point source had been attached, the fiber density was lower. This led to the belief that the fibers were being carried away with the flow. This washout effect was exacerbated closer to the point source because of the comparatively high local velocities. As the fiber density decreased, the membrane and point source could not maintain its capillary connection. Because the structural integrity of this membrane could not be maintained, a search was conducted for a rigid porous structure membrane which led to the use of the Millipore Durapore PVDF membranes. Under extended evaporation times, the membrane's integrity did not degrade. To test the membrane fouling, the membrane was forced to pump saltwater. Fouling occurred at the outer radii and progressed inward with time. As evaporation occurred from a zone where fluid had no further to travel, initially the outer radius of the membrane, the salt was left behind in the pore structure. When the solubility limit of the water was locally reached, the salt began to crystallize, blocking off that section. As such, the measured evaporation rate decreased. Eventually, the salt buildup in the membrane progressed inward to the point source, choking the flow.

From this, it can be determined that membrane fouling is based on the evaporation rates, concentration of contaminates and size of contaminates relative to the pore size.

8.1.4 Evaporative Cooling of an Externally Heated Surface

In the last experimental study, the evaporation system was subjected to loading from a light source to simulate solar loading. The evaporation system sat on a copper plate and connected to a reservoir like in the previous experiments. A halogen lamp was used to replicate solar radiation because of its similar spectrum. Additionally, cooling air could be supplied underneath the plate where the inlet and outlet temperatures were measured and calculated to cooling load. To determine the imposed load by the lamp at the test section distance, a pyranometer was used to create a 2D intensity grid. The reflectivity and absorptivity of the membrane, wet and dry, when backed by copper were measured with a spectrophotometer. The results showed that as the lamp intensity increased, with no cooling supplied to the copper plate, the evaporation rate increased. Additionally, in both the evaporating and dry membrane cases, the plate temperature increased with lamp intensity. However, even though the evaporating membrane was absorbing more energy from the lamp due to its higher absorptivity coefficient, it was able to preserve the plate temperature considerably lower than just the dry membrane. In roof applications, maintaining lower surface temperatures is important for lowering heat conduction into the structure. When cooling was applied underneath the copper plate, decreasing the plate temperature, the evaporation rate decreased. This showed that plate temperature had a dominate influence on evaporation compared to the imposed load. With that in mind, as the plate temperature was forced lower and the evaporation rate decreased, there was a point where the evaporating membrane required more cooling than the dry membrane.

8.2 Comparison with Resource Equivalent Technologies

Lastly, the resources associated with implementing the evaporation system (i.e., water, roof space, solar energy) were considered against other possible allocations. On a

typical summer day in Austin, TX, the evaporation system would use about 2 gallons/m^2/day. In contrast, those 2 gallons could go towards the producing 1 kWh of electricity which could potentially be used for air conditioning. It is believed that with roof albedos slighting over that of the tested white roof scenario, the water allocation justification would be met. When considering the installation of PV systems on the roof, there is great confidence that roof allocation spacing would favor the evaporation system rather than electricity production. Additionally, all test performed in the laboratory were done with minimal air currents. When outside, it is anticipated that air currents would cause an increase in evaporation rates and thus higher cooling capabilities.

8.3 Additionally Comments on System Operations

As demonstrated, the membrane dried out as a result of being disconnected from the reservoir by the closing of a valve. Because of this, it is important to address how the system could be restarted. Restart could possibly be achieved by using a small amount of gravity fed water from above to rewet the membrane much like the initial wetting process described in this dissertation. Additionally, perhaps wicking material could be inserted into the tubing thus allowing water to wick back to the membrane when the reservoir was reconnected.

The fouling performed in this dissertation was with a high concentration of salt. This was done to speed along the degradation process. In reality, fouling would not occur as quickly. However, with repurposed water, contamination would still exist in the water supply. It may be necessary to filter the water before it reaches the evaporation surface to remove particulates and prevent clogging of the membrane. Evaporation rates and the ability to remove contaminates from the water supply will factor into the life of the membrane and how often it might need to be replaced.

In order to scale up the size of the evaporation system to cover an entire roof, an array of point sources would need to be used. The spacing of point sources would need to be within the critical radius of evaporation; the furthest distance in the membrane a point source can deliver fluid to. Moreover, to utilize the temperature regulation of

evaporation, one would want to space the point sources a fraction of the critical radius apart. When scaled up to cover a roof, it is important to remember that different locations on that roof would have different conditions such as local wind velocities which would affect the localized evaporation rates. Another option to consider when scaling the size of the system would be to use components that would increase the thermal mass of the system. With increased thermal mass, energy could be stored within the solid phase of the porous media during periods of intense solar radiation and disposed of at times of lower radiation.

8.4 Future Directions to be Pursued

Further research should focus on implementing this system in conjunction with PV arrays. In the shade of a tilted PV array, one could receive the benefits of electricity production and enhanced cooling. Additionally, to become viable, an attempt should be made to explore a more cost effective membrane for covering a roof. It should focus on balancing energy savings against the cost and lifetime of a membrane. Furthermore, if a more cost effective membrane could not be found, attention should be paid to extending the life of the membrane through the cleaning of blockages. In further development, the point source spacing should be investigated to balance the normalized evaporation rate to the cooling capabilities. While I do not claim to eliminate the need for a building air conditioning system because there is still heat flux entering the interior, I do believe this evaporation system greatly helps in reducing the size and energy requirements of an air conditioning system. With the positive results of this investigation, it is believed that the system would not be contained to just implementation on a roof but perhaps to the building side walls as well.

Appendix A - Calibration and Uncertainty of Thermocouples

Two types of thermocouples were used throughout this dissertation, Type K and Type T. Both were calibrated in the same fashion. The thermocouples leads were connected to a National Instruments (NI) module 9211, a 4 channel, 24-bit, ±80 mV thermocouple input module. The module had a built in cold junction temperature channel. The module plugged into a NI chassis which was read by a Ni-Labview VI and recorded temperature to a spreadsheet file.

For calibration, the thermocouples were placed in a programmable chiller bath and the thermocouple reading was recorded by the VI. The VI recorded data for 10 seconds at a rate of 5 Hz and the temperature was averaged out over that time. Using a reference thermister (Fluke 1523 Reference Thermometer, ±0.003 °C accuracy) for increased accuracy, the bath temperature was recorded manually. Typically, a range of bath temperatures from 10 to 50 °C in increments of 5 °C was used for calibration.

The resulting data points were plotted with the thermister reading on the x-axis and the averaged thermocouple reading on the y-axis, Figure A.1. A linear curve fit was applied.

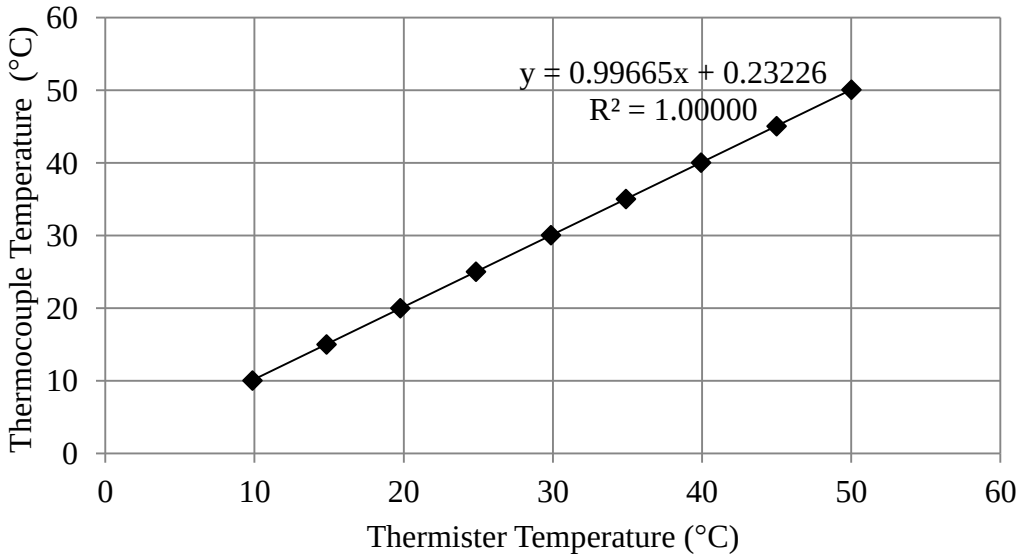

Fig. A.1: Typical calibration plot for a thermocouple.

The standard deviation was determined using Eqn. A1 [71],

$$s_n = \sqrt{\frac{1}{n-1}\sum_{i=1}^{n}(x_i - \bar{x})^2} \quad \text{(A1)}$$

where s_n is the standard deviation, n is the sample size, x_i are the measured values and $\bar{x}$ is the mean value of the measurement. From the standard deviation, the confidence deviation can be calculated using Eqn. A2,

$$Cd = t_{2,0.05,8} * \frac{s_n}{\sqrt{n}} \quad \text{(A2)}$$

where Cd is the confidence deviation and $t_{2,0.05,8}$ is the t-value being 2-tailed at a significance of 0.05 when confidence is 95% for a degree of freedom of 8. For the thermocouples, the largest calibrated uncertainty was 0.12 °C at 95% confidence.

Appendix B - Calibration and Uncertainty of Pressure Transducer

Two pressure transducers were used in this dissertation, ±34.5 kPa (Omega PX26-005DV) and ±206.9 kPa (Omega PX26-030DV) differential sensors. Both were calibrated in the same manner. The pressure transducer leads were connected to a National Instruments (NI) module 9211, a 4 channel, 24-bit, ±80 mV input module. The module plugged into a NI chassis which was read by a Ni-Labview VI and recorded voltage to a spreadsheet file.

To calibrate, one side of the pressure transducer was plugged into the bottom of a water column while the other was left open to atmosphere. The free surface of the water column could be raised to known heights above the pressure transducer up to 2 m with a resolution of 1 mm. For each height, the VI recorded data for 10 seconds at a rate of 5 Hz and the voltage output was averaged out of that time. Additionally, the height of water was converted to Pa using known properties of water. The pressure transducer's voltage was plotted against pressure and linearly fitted, Figure B.1.

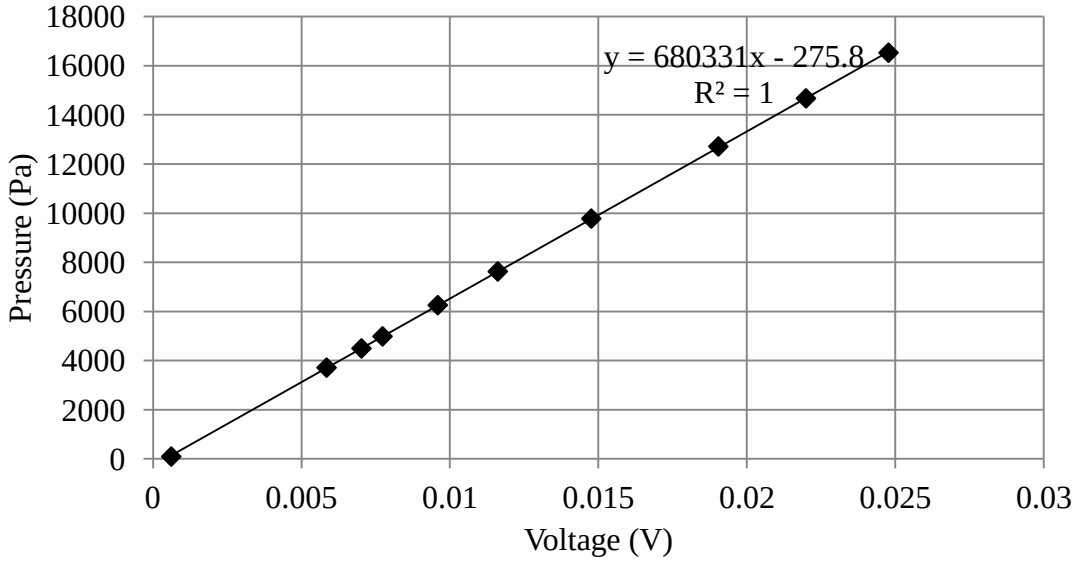

Fig. B.1: Typical calibration plot for a pressure transducer.

The uncertainty analysis was done like exampled in the thermocouple uncertainty analysis, Appendix A.1.For the transducers, the largest calibrated uncertainty was 0.03 kPa at 95% confidence.

Appendix C – Lamp Intensity Calibration

A halogen lamp (Bayco SL-1082) was used as the light source in this dissertation. To determine the intensity on the test section, located 0.43 meters beneath lamp, an Eppley precision spectral pyranometer was used to create a 2D map characterizing the flux. The pyranometer was calibrated by The Eppley Laboratory, Inc. on May 2, 2012; the minimum recommended calibration cycle was 5 years. It was calibrated under radiation intensities of approximately 700 W/m^2 but the radiometer is linear to within ± 0.5% up to 1400 W/m^2.

An intensity map for the lamps three settings (i.e., 250, 500, 750 W) was created to determine locations that would impart a uniform intensity on the test section. Uniform intensity was user defined as ± 5% of the average intensity in that spatial region and done at least every square inch. A sample intensity map for 250 W is seen in Figure C.1. The region, seen in green, is large enough to fit the test section and would impart 130 W/m^2 on it. All locations were within 3% of the average intensity.

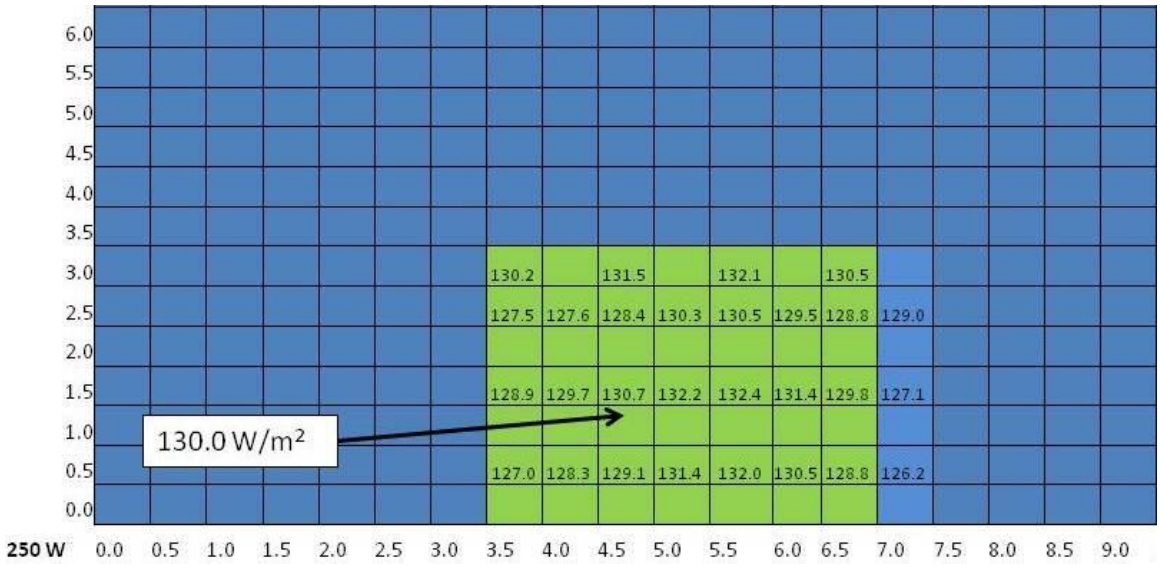

Fig. C.1: 2D intensity map with the lamp on the 250 W.

Appendix D – Calculating the Reflectivity and Absorptivity

The reflectivity for a membrane, wet and dry, when backed on copper was measured using a spectrophotometer, §5.1, for wavelengths from 350 to 2500 nm in steps of 10 nm. From those measurements, Fig. 5.3, the total reflectivity can be calculated if the irradiation is known, Eqn. D1 [64],

$$\rho = \frac{\int_0^\infty \rho_\lambda(\lambda) G_\lambda(\lambda) d\lambda}{\int_0^\infty G_\lambda(\lambda) d\lambda} \tag{D1}$$

where ρ is reflectivity, λ is wavelength, and G is irradiation. The irradiation for the halogen lamp was obtained for the different lamp powers (i.e., 250, 500, 750 W) [72]. Eqn. D1 was modified as a summation of step functions to account for the measurements every 10 nm, Eqn. D2,

$$\rho = \frac{\sum \rho_\lambda(\lambda) G_\lambda(\lambda)}{\sum G_\lambda(\lambda)}. \tag{D2}$$

The reflectivity was calculated to be 0.7 and 0.92 for the wet and dry membrane on copper, respectively. To calculate absorptivity, the reflectivity must be subtracted from unity, Eqn. D3,

$$\alpha = 1 - \rho \tag{D3}$$

where α is the absorptivity. Note that there was no transmission through the copper and membrane. The absorptivity was calculated to be 0.3 and 0.08 for the wet and dry membrane on copper, respectively.

Appendix E – Thermal Assumptions Validation

In both Chapters 4 and 5, copper plates were used as substrates for the evaporation system. In Chapter 4, heaters were placed on the underside of the plate while in Chapter 5, a lamp imparted a heat flux from above. In both studies, thermocouples were placed at various locations in the copper plate. A sampling of the uniformity of their temperatures can be seen in Figure E.1. The constant plate temperature can be seen when evaporation was occurring with no air cooling underneath with the lamp imparting 315 W/m^2. This type of behavior was typical for experiments in both chapters.

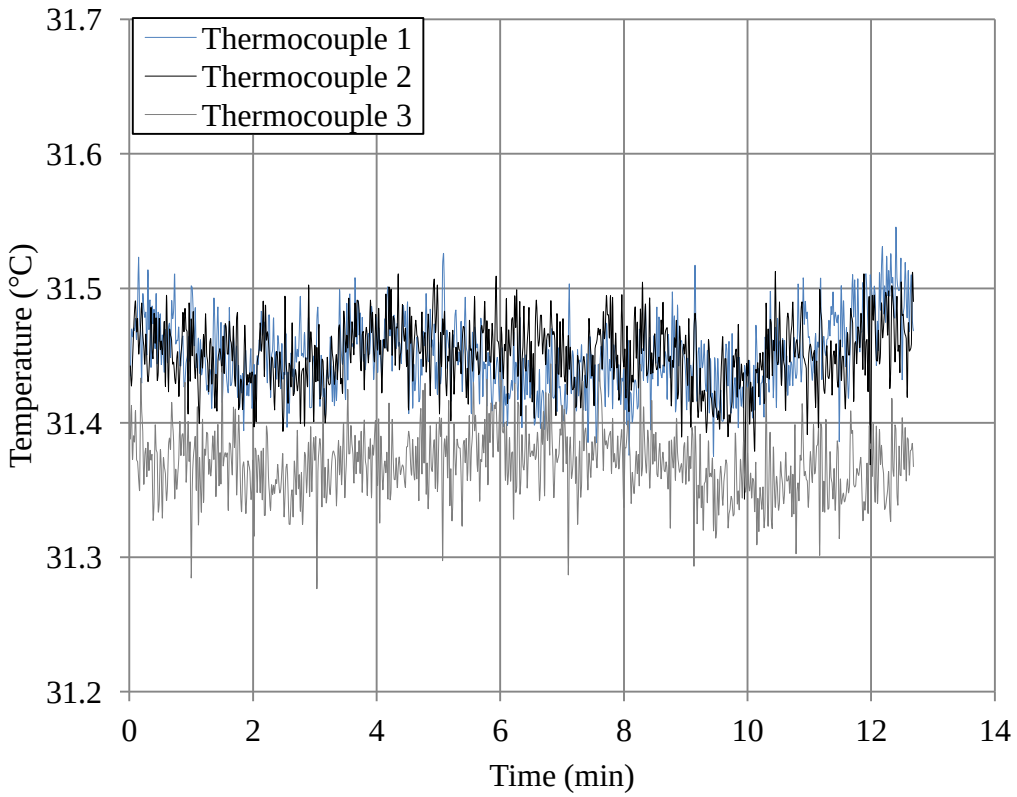

Fig. E.1: Constant plate temperature was observed with thermocouples places at different locations in the plate. From Chapter 5, evaporation was occurring with no cooling assistance for a lamp intensity of 315 W/m^2.

Appendix F – Heat Loss through Insulation Validation

In both Chapters 4 and 5, copper plates were used as substrates for the evaporation system. Those substrates were insulated with alumina-silica which had a thermal conductivity of 0.025 W/m/K [73]. To determine the heat loss through the insulation by conduction, the temperatures in the plate as well as 5 cm below the plate were measured.

The highest power that was to be tested for evaporation experiments was supplied to the heater. This amounted to ~4.8 W or 272 W/m^2. The temperatures in the plate and beneath the insulation were 52 and 28 °C, respectively. These values were applied to the heat conduction equation, Eqn. F1 [64],

$$q_{calc} = \frac{-k*(T_{ins}-T_{plate})}{x} \quad \text{(F1)}$$

where q_{calc} is the calculated heat flux related to conduction, k is the thermal conductivity of the insulation, T_{ins} is the temperature measured in the insulation, T_{plate} is the plate temperature and x is thickness of the insulation. The heat flux from conduction equated to 11.8 W/m^2 or ~4.3% of the total heat flux.

References

[1] Schmitt, O., 1969, "Some interesting and useful biomimetic transforms," Third International Biophysics Congress, pp. 297.

[2] Vincent, J., Bogatyreva, O., Bogatyreva, N., Bowyer, A., and Pahl, A., "Biomimetics: its practice and theory," Journal of the Royal Society Interface, **3** (9), pp.471–482.

[3] Roth-Nebelsick A., Uhl D., Mosbrugger V., and Kerp H., 2001, "Evolution and Function of Leaf Venation Architecture: A Review," Annals of Botany, **87**(5), pp. 553–566.

[4] Campbell, N., and Reece, J., 2008, *Biology*, Pearson Benjamin Cummings, San Francisco, CA, Chap. 36

[5] Lange O. L., 1959, "Untersuchungen über Wärmehaushalt und Hitzeresistenz mauretanischer Wüsten- und Savannenpflanzen," Flora **147**, pp. 595-651.

[6] Lange O. L., 1963, "Die Photosynthese der Flechten bei tiefen Temperaturen und nach Frostperioden," Ber. dt. bot. Ges. **75**, pp. 351-352.

[7] Dixon H., and Joly J., 1895, "On the ascent of sap," Philosophical Transactions of the Royal Society of London. B, **186**, pp. 563–576.

[8] Zwieniecki M., Melcher P. J., Boyce C. K., Sack L., and Holbrook N. M., 2002, "Hydraulic architecture of leaf venation in Laurus nobilis L.," Plant, Cell and Environment, **25**(11), pp. 1445–1450.

[9] Wheeler, T. D., and Stroock A. D., 2008, "The transpiration of water at negative pressures in a synthetic tree.," Nature, **455**(7210), pp. 208–12.

[10] Goedecke N., Eijkel J., and Manz A., 2002, "Evaporation driven pumping for chromatography application.," Lab on a chip, **2**(4), pp. 219–23.

[11] Zimmermann U., Meinzer F. and Bentrup F., 1995, "How does water ascend in tall trees and other vascular plants?," Annals of Botany, **76**, pp. 545–551.

[12] Nobel, P.S., 1983, *Biophysical plant physiology and ecology.* W. H. Freeman and Company, New York, NY.

[13] Sachs, J., 1987, *Vorlesungen über Pflanzen-physiologie.* Leipzig: Verlag Wilhelm Engelmann.

[14] Plumb, R., and Bridgman, W., 1972, "Ascent of sap in trees," Science, **179**, pp. 1129–1131.

[15] Zimmermann, U., Zbu, J., Meinzer, F., Goldstein, G., Schneider, H., Zimmermann, G., Benkert, R., Thürmer, F., Melcher, P., Webb, D., and Haase, A., 1994b, "High molecular weight organic compounds in the xylem sap of mangroves: implications for long-distance water transport," Botanica Acta, **107**, pp. 218–229.

[16] Cary, J., Jensen, M., and Fisher, H., 1968, "Physical state of water in plat xylem vessels," Agronomy Journal, **60**, 167–169.

[17] Amin, M., 1982, "Ascent of sap in plants by means of electrical double layers," Journal of Biological Physics, **10**, pp. 103–109.

[18] U.S. Energy Information Administration, 2012, "Annual Energy Review 2011," DOE/EIA-0384(2011).

[19] U.S. Department of Energy, 2010, *Buildings Energy Data Book*, 3.1 Commercial Sector Energy Consumption. (http://buildingsdatabook.eren.doe.gov/TableView.aspx?table=3.1.4).

[20] Kimura K., Yamato N., Yamamura H., and Watanabe Y., 2005, "Membrane fouling in pilot-scale membrane bioreactors (MBRs) treating municipal wastewater.," Environmental science & technology, **39**(16), pp. 6293–9.

[21] Chiou Y.-T., Hsieh M.-L., and Yeh H.-H., 2010, "Effect of algal extracellular polymer substances on UF membrane fouling," Desalination, **250**(2), pp. 648–652.

[22] Tracey, E., and Davis, R., 1994, "Protein fouling of track-etched polycarbonate microfiltration membrane," Journal of Colloid and Interface Science, **167**, pp. 104–116.

[23] Darcy, H., 1856 *Les Fontaines Publiques de la Ville de Dijon*, Dalmont, Paris.

[24] Washburn, E., 1921, “The dynamics of capillary flow,” Physical Review, **17**(3), pp.273–283.

[25] Waghmare P. R., and Mitra S. K., 2012, “A comprehensive theoretical model of capillary transport in rectangular microchannels,” Microfluidics and Nanofluidics, **12**, pp. 53–63.

[26] Waghmare, P.R., Mitra, S.K., 2010a, “Finite reservoir effect on capillary flow of microbead suspension in rectangular microchannels,” J Colloid Interface Sci, **351**(2) pp.561–569.

[27] Waghmare, P.R., Mitra, S.K., 2010b, “Modeling of combined electroos- motic and capillary flow in microchannels“ Anal Chim Acta, **663,** pp.117–126.

[28] Diotallevi, F., Biferale, L., Chibbaro, S., Pontrelli, G., Toschi, F., Succi, S., 2009, “Lattice boltzmann simulations of capillary filling: finite vapour density effects,” Eur Phys J, **171**(1), pp.237–243.

[29] Zhang, J., 2011, “Lattice boltzmann method for microfluidics: models and applications,” Microfluid Nanofluid, **10,** pp.1–28.

[30] Dimitrov, D., Milchev, A., Binder, K., 2007, “Capillary rise in nanopores: Molecular dynamics evidence for the lucas-washburn equation,” Phys Rev Letters, **99**, pp.054501.

[31] North, M., 2013, “Optimization of heat pipe thermal transport using axially graded capillary wick structures,” Proc. ASME International Mechanical Engineering Congress and Expo, Orlando, FL, IMECE2005-82950, pp. 1–8.

[32] Camassel B., Sghaier N., Prat M., and Ben Nasrallah S., 2005, “Evaporation in a capillary tube of square cross-section: application to ion transport,” Chemical Engineering Science, **60**(3), pp. 815–826.

[33] Araujo, A., Song, Y., Lundeberg, J., Stahl, P., and Brumer, H., 2012, “Activated paper surfaces for the rapid hybridization of DNA through capillary transport,” Anal. Chem., **84**, pp.3311−3317.

[34] Laser D. J. and Santiago J. G., 2004, “A review of micropumps,” Journal of Micromechanics and Microengineering, **14**(6), pp. R35–R64

[35] Limbach P. A. and Meng Z., 2002, "Integrating micromachined devices with modern mass spectrometry," The Analyst, **127**(6), pp. 693–700.

[36] Tuckerman D. B. and Pease R. F. W., 1981, "High-Performance Heat Sinking for VLSI," IEEE Electron Device Letters, **EDL-2**(5), pp. 126–129.

[37] Jiang L., Mikkelsen J., Koo J., Huber D., Yao S., Zhang L., Zhou P., Maveety J. G., Prasher R., Santiago J. G., Kenny T. W., and Goodson K. E., 2002, "Closed-Loop Electroosmotic Microchannel Cooling System for VLSI Circuits," IEEE Trans. Compon. Packag. Technol., **25**(3), pp. 347–355.

[38] Zhang L., Koo J., Jiang L., Asheghi M., Goodson K. E., Santiago J. G., and Kenny T. W., 2002, "Measurements and Modeling of Two-Phase Flow in Microchannels With Nearly Constant Heat Flux Boundary Conditions," Journal of Microelectromechanical Systems, **11**(1), pp. 12–19.

[39] Borno R., Steinmeyer J., and Maharbiz M., 2009, "Charge-pumping in a synthetic leaf for harvesting energy from evaporation-driven flows," Applied Physics Letters, **95**, pp. 013705(1-3).

[40] Namasivayam V., Larson R. G., Burke D. T., and Burns M. A, 2003, "Transpiration-based micropump for delivering continuous ultra-low flow rates," Journal of Micromechanics and Microengineering, **13**(2), pp. 261–271.

[41] Guan Y.-X., Xu Z.-R., Dai J., and Fang Z. L., 2006, "The use of a micropump based on capillary and evaporation effects in a microfluidic flow injection chemiluminescence system.," Talanta, **68**(4), pp. 1384–9.

[42] Xu Z., Zhong C., Guan Y., Chen X., Wang J., and Fang Z. L.., 2008, "A microfluidic flow injection system for DNA assay with fluids driven by an on-chip integrated pump based on capillary and evaporation effects," Lab on a chip **8**(10), pp. 1658-1663.

[43] Li J., Liu C., Xu Z., Zhang K., Ke X., Li C., and Wang L., 2011, "A bio-inspired micropump based on stomatal transpiration in plants.," Lab on a chip, **11**(16), pp. 2785–9.

[44] Simpson J. R., and McPherson E. G., 1997, "The effects of roof albedo modification on cooling loads of scale model residences in Tucson, Arizona," Energy and Buildings, **25**(2), pp. 127–137.

[45] Akbari H. and Matthews H. D., 2012, "Global cooling updates: Reflective roofs and pavements," Energy & Buildings, **55**, pp. 8–12.

[46] Cheikh, H. B., and Bouchair, A., 2004, "Passive cooling by evapo-reflective roof for hot dry climate," Renewable Energy, **29**, pp.1877-1886.

[47] Chen W., and Liu W., 2010, "Thermal analysis on the cooling performance of a porous evaporative plate for building," Heat Transfer-Asian Research, **39**(2), pp. 127–140.

[48] Al-Turki, and A., Zaki, G., 1991, "Energy saving through intermittent evaporative roof cooling," Energy and Buildings, **17**, pp. 35–42.

[49] Sodha, M., Mahajan, U., and Sawhney, R., 1993, "Thermal performance of roof evaporative cooling and floor coupled evaporatively cooled underground water storage tank systems," International Journal of Energy **17**(2), pp. 127–140.

[50] Wanphen S., and Nagano K., 2009, "Experimental study of the performance of porous materials to moderate the roof surface temperature by its evaporative cooling effect," Building and Environment, **44**(2), pp. 338–351.

[51] Pagliarini G., and Rainieri S., 2011, "Dynamic thermal simulation of a glass-covered semi-outdoor space with roof evaporative cooling," Energy and Buildings, **43**(2-3), pp. 592–598.

[52] Sethi, V., Sharma, S., 2007, "Survey of cooling technologies for worldwide agricultural greenhouse applications," Solar Energy, **81**(12), pp. 1447–1459.

[53] M.S. Sodha et.al, 1986, *Solar Passive Building: Science and Design*, Pergamon press, U.K.

[54] Giacomelli, G.A., and Roberts, W., 1989. Try alternative methods of evaporative cooling. Acta Horticulturae, **257**, 29–41.

[55] Mannan, K., and Cheema, L., 1979, "Year-round studies on natural cooling and heating of green houses in northern India," Proc. International Solar Energy Society, Atlanta, GA, **2**, pp.1699-1703.

[56] Lawrence Berkeley Nation Laboratory, 2000. "Cool Roofing Materials Database," (http://energy.lbl.gov/coolroof/)

[57] J. Rhodes, V. Raman, M. Webber, 2012, "Solar radiation for August 2, 2012, Austin, TX".

[58] Torcellini, P., Long, N., and Judkoff, R., 2003, "Consumptive water use for U.S. power production," TP-550-33905, National Renewable Energy Laboratory, Golden, CO.

[59] American Society of Heating, Refrigeration and Air-Conditioning Engineers, 2001, *ASHRAE Handbook Fundamentals*, American Society of Heating, Refrigeration and Air-Conditioning Engineers, Inc. Atlanta, GA.

[60] Kuitche J. M., Sharma V., Oh J., Pan R., TamizhMani G., 2012, "Statistical Analysis of Commercial c-Si PV Module Photovoltaic Efficiency Distribution over 10-Years Period," 38th IEEE Photovoltaic Specialists Conference, Mesa, AZ, pp. 2421–2425.

[61] Dominguez A., Kleissl J., and Luvall J. C., 2011, "Effects of solar photovoltaic panels on roof heat transfer," Solar Energy, **85**(9), pp. 2244–2255.

[62] Feldman, D., Barbose, G., Margolis, R., Wiser, R., Darghouth, N., and Goodrich, A., 2012, "Photovoltaic (PV) pricing trends: historical, recent, and near-term projections, Department of Energy, National Renewable Laboratory and Lawrence Berkeley National Laboratory, DOE/GO-102012-3839.

[63] Rohwer, C., 1931, "Evaporation from free water surface," US Department of Agriculture, Bulletin 271.

[64] Incropera, F., et al. 2007, *Fundamentals of Heat and Mass Transfer*, 6th edition, John Wiley & Sons, Hoboken, NJ.

[65] Smith, C., Jones, R., and Lof, G., 1993, "Energy requirements and potential savings from heated indoor swimming pools," ASHRAE Transactions, **99**(2), pp. 864-974.

[66] Biasin, K., and Krumme, W., 1974, "Die wasserverdunstung in einem innenschwimmbad," Electrowaerme International, **32**(A3), pp. A115-129.

[67] Boelter, L., Gordon, H., and Griffin, J., 1946, "Free evaporation into air of water from a free horizontal quiet surface," Industrial & Engineering Chemistry, **38**(6), pp. 596-600.

[68] Himus, G., and Hichley, J., 1924, "The effect of a current of air on the rate of evaporation of water below the boiling point," Chemistry and Industry, **22**, pp. 840-845.

[69] Leven, K., 1969, "Betrag zur frage der wasserverdunstung," Waerme-und Kaeltetechnick, **44**(11), pp. 161-167.

[70] Box, T., 1876, *A Practical Treatise on Heat*, E & FN Spon, New York.

[71] Currell, G., and Dowman, A., 2009, *Essential Mathematics and Statistics for Science*, 2nd edition, Wiley-Blackwell, West Sussex, UK.

[72] Oriel, 2013, "Oriel product training," Newport, Stanford, CT, pp. 1–39.

[73] Alibaba, "Aluminium silicate insulation," (http://www.alibaba.com/product-gs/363963062/Aluminium_silicate_Insulation.html?s=p).

Vita

Robert Crawford attended La Salle College High School, Wyndmoor, PA. In 2004, he enrolled at Villanova University, Villanova, PA, pursing a degree in mechanical engineering. Upon graduating, he remained at Villanova University to obtain a master's degree in mechanical engineering. Beginning in 2011, he studied at The University of Texas at Austin. In 2013, he graduated with a Ph.D. in mechanical engineering.

This manuscript was typed by Robert Crawford.